

SILICON NITRIDE DEVICES FOR NONLINEAR AND QUANTUM OPTICS
APPLICATIONS

by

SARATH CHANDRA SAMUDRALA

Presented to the Faculty of the Graduate School of
The University of Texas at Arlington in Partial Fulfillment
of the Requirements
for the Degree of
DOCTOR OF PHILOSOPHY

THE UNIVERSITY OF TEXAS AT ARLINGTON

May 2016

Copyright © by SARATH CHANDRA SAMUDRALA 2016

All Rights Reserved



ACKNOWLEDGEMENT

First I would like to express my deep thankfulness to Professor Michael Vasilyev for giving me this great opportunity to work with him in his group and advising me with patience. Professor Vasilyev is an extremely talented researcher, with a very strong theoretical understanding with brilliant experimental knack and skills which is an extremely rare combination. Almost after every interaction I had with Professor Vasilyev, my understanding on concepts deepened and my ability to address minute experimental details improved enormously. His constant inquisitive mind will be a great inspiration to me for the rest of my life. I am also very much thankful for his understanding and support during times of my personal difficulties.

I would also like to thank Professor (Late) Nikolai Stelmakh with whom we had collaborations in various projects. His unfortunate sudden demise had a deep impact on the project and it was never easy to recover thereafter. Professor Stelmakh's expertise on wide variety of topics in RF electronics, photonics and microfabrication, and his ingenious problem solving abilities have a lifetime impact on me.

I would also like to thank Professor Robert Magnusson , Professor Seong Jin Koh, Professor Weidong Zhou, and Professor Alice Sun for accepting my request

to be on my PhD committee and giving me valuable suggestions on my dissertation.

I am also very thankful to the Shimatzu Institute of Nano Technology Research center staff, Dr Nader Hozhabri, Mr. Dennis Bueno, Mr. Richard K. Chambers, Mr. Paul Logan and former engineer Mr. Richard Wells for their help during the fabrication process.

I am very thankful to my father Dr Manohar, mother Sharada, and my brother Subhash Chandra for their constant support from thousands of miles away.

It is not an overstatement to say that my PhD would never have been possible without the patience and constant encouragement from my wife Kalyani, throughout the program. Her strength and support during many years of long and late night working hours in the laboratory is an exemplary demonstration of what it means to be a life partner.

I also would like to extend my deep gratitude to my fellow group members Lu Li and Young Kwon for helping me in the laboratory, and former members Muthu Annamalai and Lei Zhu for their collaboration, support and suggestions during my research. I also would like to thank and wish best of luck to all my group members Subrata Das, Kamanashis Saha, Afshin, Rouf and former member Mohan.

May 1 2016

ABSTRACT

SILICON NITRIDE DEVICES FOR NONLINEAR AND QUANTUM OPTICS
APPLICATIONS

Sarath Chandra Samudrala , PhD

The University of Texas at Arlington, 2016

Supervising Professor: Michael Vasilyev

The technology of fabricating photonic devices on silicon wafers using the well established CMOS process methodology has been under active investigation for several years. In particular, microring resonators have been shown to have several applications in telecommunications, in sensors and in nonlinear and quantum optics.

This dissertation presents theoretical details and experimental results of silicon-nitride-based microring resonators fabricated on silicon wafers. The theoretical details of optical waveguides and numerical simulations of submicron thick waveguides are discussed. Later, the fabrication details of microring

resonators and the experimental results of transmission properties of these microrings are presented.

Further, the dispersion in microrings is experimentally investigated and the measured dispersion values are presented. The fabricated microring resonator with a simple coupler showed a dispersion value of -2000 ps/nm-km. A novel approach for compensating the dispersion by using a dispersive asymmetric Mach-Zehnder interferometer coupler is proposed and the corresponding microring device is fabricated. The experimental results of this scheme show the absolute value of the residual dispersion of less than 100 ps/nm-km, indicating significant dispersion compensation by our approach.

Table of Contents

Acknowledgement.....	iii
Abstract.....	v
List of Figures.....	ix
List of Tables.....	xii
Chapter 1 Introduction.....	1
1.1. Materials & Devices.....	3
1.1.1 $\chi^{(3)}$ materials and nonlinear optics.....	5
1.2 Microring Resonators for Nonlinear and Quantum Optics.....	7
1.3 Outline of the Thesis.....	8
Chapter 2 Theory of optical waveguides and microring resonators.....	9
2.1 Theory of optical waveguides.....	9
2.2 TE, TM and Quasi TE, TM modes.....	12
2.3 Microring Resonators.....	20
2.4 Operating regimes of resonators.....	23
2.5 Parameters characterizing the ring resonators.....	26
2.6 Summary.....	27
Chapter 3 Fabrication and characterization of microrings.....	28
3.1 E-beam lithography process.....	30
3.2 Reactive Ion Etching.....	37
3.3 Characterization setup.....	43

3.4 Experimental results.....	45
3.5 Characterization of the delay-line properties of microrings.....	49
3.6 Summary.....	52
Chapter 4	
Asymmetric Mach-Zehnder Interferometer based microring resonator.....	53
4.1 Mode spacing in a microresonator.....	54
4.2 Experimental results.....	62
4.3 Summary.....	66
Chapter 5 Conclusion.....	67
Appendix A Pulse picker driver for Pockels cell.....	69
A.1 Description of the pulse generator.....	71
A.2 Frequency divider PCB.....	72
A.3 RF amplifier.....	73
A.4 Frequency divider.....	74
A.5 High-voltage amplifier PCB.....	75
A.6 Voltage regulator PCB.....	78
A.7 Bias-control PCB.....	78
A.8 Power supplies and chassis of the box.....	79
A.9 Conclusion.....	80
References.....	82

List of Illustrations

Figure 2-1. A side cross-section of a simple slab waveguide where a higher refractive index material n_c is surrounded by two lower refractive indices of n_s ..	12
Figure 2-2. (a) A slab waveguide supporting TE mode. (b) A slab waveguide showing the propagation of a TM mode.....	14
Figure 2-3. A channel waveguide with core buried in the cladding of refractive index n_2	16
Figure 2-4. Simulated mode profiles in the channel waveguide.....	18
Figure 2-5. Simulated mode profiles for a thicker core in a channel waveguide.	19
Figure 2-6. Cartoon showing the micro ring resonator with coupling coefficient τ and the reflection coefficient ρ	21
Figure 2-7. Plot showing the resonator in different operating regimes.....	25
Figure 3-1. Fabrication process flow.....	34
Figure 3-2. SEM images of a part of the pattern before etching. (a) Without baking the resist. (b) Cross-section after baking the resist to reflow. Image taken after FIB milling of the cross-section.....	36
Figure 3-3. Process of reactive ion etching.....	38
Figure 3-4. SEM micrographs. (a) Waveguide cross section. (b) Gap between the microring and the bus waveguide. (c) Microring resonator.....	42
Figure 3-5. Schematic of the characterization setup.....	43
Figure 3-6. Free spectral range plot of the microring resonator with FSR value 2.15 nm.....	45
Figure 3-7. Full width at half-minimum of 80 pm of one of the resonances.....	46
Figure 3-8. Experimental data of a critically coupled microring resonator.....	48

Figure 3-9. Experimental data of a microring resonator in an under-coupled regime.	48
Figure 3-10. Experimental setup for investigating delay-line properties of a microring.....	49
Figure 3-11. (a) Pulse positions at OFF resonance. (b) Pulse position at ON Resonance.....	51
Figure 4-1. (a) Microresonator with simple input / output coupler, described by Eq. (4.1). (b) Similar microresonator, in which simple coupler has been replaced by a more general four-port coupler, which may have frequency-dependent amplitudes and phases of the coupling and reflection coefficients.....	54
Figure 4-2. (a) Definition of coupling and reflection coefficients of a general four-port coupler. (b) Implementation of a four-port coupler by an asymmetric Mach-Zehnder interferometer (AMZI) with ΔL path difference between its two arms.....	55
Figure 4-3. Modeling results of the change in the free spectral range for different resonances (blue curve), with red dots representing a microresonator with a simple coupler. Parameters (a) $N=31$ and $T=0.13$. (b) $N=61$ and $T=0.3$	61
Figure 4-4 (a) Transmittance of the microresonator (solid black), power coupling coefficient $ \kappa_{14} ^2 = 1- \rho_{24} ^2$ of the AMZI coupler (dashed blue), and normalized dispersion of the AMZI coupler $D_{\text{compensated}} / (2D)$ (dot-dashed red), obtained with $D = -2000$ ps/nm/km, $\Delta\nu_{\text{FSR}} = 200$ GHz, $\lambda = 1550$ nm, $n_g \approx 1.6$, $\varepsilon = 0.1$, $N = 34$, and $T = 0.13$	63
Figure 4-4 (b) Experimentally measured spectrum of the transmittance of a Si_3N_4 microresonator with AMZI coupler, with $\Delta\nu_{\text{FSR}} \approx 180$ GHz and $N \approx 50$. Normalized frequency detuning θ is defined by Eq. (4.16).....	63
Figure 4-5. (a) Frequency spacings $\Delta\nu_{\text{FSR}}$ for a Si_3N_4 microresonator with a simple coupler, indicating waveguide dispersion $D \approx -2000$ ps/nm/km. (b) Frequency spacings $\Delta\nu_{\text{FSR}}$ for a Si_3N_4 microresonator with AMZI coupler with $N \approx 30$	64

Figure 4-6. (a) Scanning electron microscope (SEM) images of fabricated Si ₃ N ₄ microresonators with AMZI couplers and different length differences between the long and short arms ΔL . (b), (c) SEM and optical microscope images of the fabricated Si ₃ N ₄ microresonator with an AMZI coupler after deposition of the heating electrodes used for separate tuning of the AMZI and the microresonator.....	65
Figure A-1. Schematic of operation of pulse picker.....	70
Figure A-2. Schematic for the RF amplifier circuit to amplify the output from monitor photodiode of the laser.....	73
Figure A-3. Circuit schematics of frequency dividers.....	75
Figure A-4. Schematic showing transistors in complimentary scheme.....	76
Figure A-5. Schematic showing MOSFETS generating high voltage.....	77
Figure A-6. Schematic showing the bias-control PCB.....	79
Figure A-7. Photograph showing the pulse on the oscilloscope.....	80

List of Tables

Table 1-1 Table showing losses and material symmetry of different materials.....	4
Table 3-1 TRION DRIE Process parameters.....	39

CHAPTER 1

INTRODUCTION

Photonics has revolutionized the technology of telecommunications and has become a part of our everyday lives. A variety of advances, from realization of transatlantic communications to internet carrying high speed data containing high definition voice and video content, have been made possible with this technology which involves a combination of optical fibers, optical sources, detectors, modulators and high-speed electronics. The efforts to miniaturize these components onto a chip scale started in late 1960's and in early 70's [1–3], which formed the early foundation in the technology of integrated optics, the term that has been traditionally used to describe the optical components fabricated on a single platform. The miniaturization comes with the several advantages such as large bandwidths (because of optical frequencies), immunization from electromagnetic interferences, inexpensive, small size, and light weight. One of the major applications of integrated optics technology is the possibility of integrating this with electronic circuits on a silicon chip. Since data rates of the signals in telecommunications and computation applications have been increasing decade after decade, the density of electronic circuits per chip has been growing in agreement with Moore's law [4]. At high data rates the copper interconnects in

these circuits suffer from several limitations due to cross talk between the connecting traces and thermal management challenges due to high density. This led to the investigation into the idea of combining photonic interconnects and components on silicon platforms along with electronics and fabricating them together, utilizing the well established CMOS process flow cycles. This technology in modern times is referred to as Photonic Integrated Circuits (PICs), silicon photonics, Integrated photonics or Nanophotonics (term especially used to define the interaction of light and matter at nanoscale dimensions on a photonic chip), with obscure distinctions. With the development of advanced lithography and etching techniques, significant progress also has been made in recent times [4–10] with a goal including the reduction of the device footprint and the energy required per bit. Several integrated photonic devices on silicon substrates have been reported, such as modulators [11–14] and multiplexers/demultiplexers [15–18], which are mostly photonics-only devices, but can also be integrated with electronics on a chip with either interface or a monolithic fabrication methods for high-speed processing applications.

Photonics chip technology suffers coupling losses between photonic waveguides which have mode areas less than $0.5 \mu\text{m}^2$ and standard optical fibers with mode areas about $50 \mu\text{m}^2$, and considerable research is also being done towards reducing these losses [19–22].

1.1 Materials & Devices

The choice of materials for photonic integrated circuits (PICs) is a subject of extensive research, and the materials used for integrated electronic circuits demonstrate great usability for photonic applications in linear optics and nonlinear optics applications. Some of the most investigated materials are Si_3N_4 (Silicon nitride), Si (Silicon, Silicon-On-Insulator), SiON (Silicon oxynitride), SiGe (Silicon Germanium), Hydrex glass, and Aluminum nitride. It appears that these materials promise to be very attractive choice for photonic integrated circuit technology.

Few of the important factors considered in choosing the materials are the propagation loss of the material, type of the nonlinearity, nonlinear properties (for higher-power applications at the wavelengths of interest) and CMOS process flow compatibility.

The following table shows the symmetry of the material and reported loss of waveguides made from seven different materials that are being investigated intensely.

Material	Loss(1550nm)	$\chi^{(2)}$	$\chi^{(3)}$	References
Si ₃ N ₄	0.08–0.09 dB/cm		✓	[23]
hydrex	0.06 dB/cm		✓	[24]
AlN	0.6dB/cm	✓	✓	[25], [26]
SiON	1.6dB/cm		✓	[27]
Si	0.026 dB/cm		✓	[28]
SiGe	0.5-5 dB/cm		✓	[29]
a-Si-H	2 dB/cm		✓	[30]

Table 1-1: Table showing losses and material symmetry of different materials

It has been shown that, with these materials, it is quite possible to make not just optical waveguides, but also passive and active devices such as splitters, modulators, resonators, and photodiodes. All these devices can be fabricated monolithically or by hybrid integration methods.

The material Silicon (Si) has been a major choice for short-distance interconnects between, e.g., a microprocessor and memory. But it has several disadvantages such as high waveguide sidewall scattering losses (due to large index contrast), coupling losses during coupling into a fiber and its inability to be an efficient material for nonlinear-optical applications because of two-photon absorption (TPA). A practical alternative option is Silicon nitride with major

advantages such as low propagation loss and negligible absorption due to its large bandgap.

Silicon nitride has been an excellent material as an insulator in transistors and MOSFETs. But its applications as an optical material are relatively recent. Silicon nitride is a $\chi^{(3)}$ material, meaning it is centrosymmetric and has applications in both linear and nonlinear optics, as well as in quantum optics.

1.1.1 $\chi^{(3)}$ materials and nonlinear optics

Nonlinear optical properties of $\chi^{(3)}$ materials have several applications in optical signal processing. Such materials with the potential for photonic integration include silicon (amorphous & crystalline forms), silicon dioxide, silicon nitride (SiN), a-Si-H (amorphous hydrogenated silicon), AlGaAs, chalcogenide glass, hydrex glass. Among these the most CMOS compatible one Si, a-Si-H and SiN.

Since the current, well established CMOS technology is solely developed for the material silicon, it proposes to be a natural choice. Moreover silicon has low linear absorption coefficient between 1260 nm to 1670 nm and has good nonlinear refractive index of $n_2 \approx 4.0 \times 10^{-14} \text{ cm}^2 / \text{W}$ [31]. The bandgap energy of silicon is 0.79 eV. Thus, two such photons will have sufficient energy to cross the bandgap of silicon and will get easily absorbed. This effect is called two-photon

absorption, and the absorbed photons generate free carriers with large life times [32].

The a-Si-H is a good material choice, which can be deposited at temperatures less than 400°C and thus can be post-processed with back-end electronics present. Its half-bandgap is less than 0.85 eV, and thus TPA should not occur. But the studies [33] have shown that high pump powers would degrade this material and thus decrease the efficiencies of the nonlinear-optical effects.

The material Silicon nitride promises to be a very practical alternative. Its refractive index is ~ 2.0 , and therefore it can have high mode confinement enabling smaller effective area ($\sim 0.5 \mu\text{m}^2$), which enhances nonlinear-optical phenomena. Even though its nonlinear refractive index $n_2 = 2.5 \times 10^{-15} \text{ cm}^2/\text{W}$ is lesser than silicon, there are no TPA effects because of large bandgap (5 eV) [34].

1.2 Microring Resonators for Nonlinear and Quantum Optics

The nonlinear interaction of the electromagnetic wave with the material not only depends upon the nonlinear coefficient of the material and the effective cross-sectional area of the waveguide, but also on the resonant structures of the

waveguides, in which case enormous amount of field and intensity buildup can be obtained in high-finesse cavities. One of the most interesting device structures for such applications are microring resonators, which are circular waveguides in which enormous energy build up can be obtained when the input field is in resonance with the resonator modes. Such devices have been exploited to generate frequency combs [35–44], where equally spaced new wavelengths can be generated. Also these microring cavities can be utilized to generate entangled photon pairs [45–47] that can be used in the areas of quantum communications and quantum cryptography. In the process of generation of photon pairs, the pump frequency is aligned with one of the ring cavity modes, and the photon pairs can be obtained at other cavity modes, as long as the phase matching is maintained. This process of the generation of a frequency comb and the number of frequencies generated depend upon the dispersion in the microring resonators, which makes the free spectral range (the spacing) between the resonant modes of the microresonator to become unequal.

1.3 Outline of the Thesis

This thesis first discusses the Silicon nitride waveguide simulations and theory behind microring resonators in Chapter 2. The details about the fabrication methodology of microrings and their characterization results are then presented in

Chapter 3. The thesis further proceeds into Chapter 4 that discusses the dispersion measurements, introduces a novel methodology by which the dispersion can be compensated, and presents our experimental results in that effort. Chapter 5 summarizes the results. Appendix A discusses the details of the home-built Pulse Picker sub-system, which, although not directly related to silicon-nitride fabrication, can still be used for high-peak-power characterization of integrated photonics devices and nanophotonic structures.

CHAPTER 2

THEORY OF OPTICAL WAVEGUIDES AND MICRORING RESONATORS

2.1 Theory of optical waveguides

The origin of the idea of routing optical signals on an integrated optics chip consisting of dielectric waveguides originated in 1960s [48, 49]. The research on such photonic structures involved a thin dielectric film deposited by chemical vapor deposition (CVD) techniques which acts as a guiding layer (core) and the material surrounding this is cladding which separates the substrate from the core avoiding the leakage of electromagnetic energy [50]. The basic theory behind the propagation of electromagnetic energy in such structures can be described starting from Maxwell's equations.

If such a medium is source free ($\rho=0$) and if the medium is dielectric ($J=0$, i.e., no surface currents, unlike in metallic waveguides), ϵ and μ are independent of electric field meaning the medium is linear and also is isotropic, then the Maxwell's equations can be written as

$$\nabla \times \vec{E} = -\frac{\partial \vec{B}}{\partial t} \quad (2.1)$$

$$\nabla \times \vec{H} = -\frac{\partial \vec{D}}{\partial t} \quad (2.2)$$

$$\nabla \cdot \vec{D} = 0 \quad (2.3)$$

$$\nabla \cdot \vec{B} = 0 \quad (2.4)$$

The flow of the energy in such structures happens by the oscillations of the dipoles in the dielectric structures.

The first two equations are coupled first-order differential equations in which one physical quantity is dependent on the other. The two equations are decoupled by taking curl on both sides and are converted into single second-order differential equations [51]:

$$\nabla \times (\nabla \times \vec{E}) = \nabla \times \frac{-\partial \vec{B}}{\partial t} = \nabla \times \frac{-\partial \mu \mu_0 \vec{H}}{\partial t}, \quad (2.5)$$

$$\nabla \times \nabla \times \vec{E} = -\mu \mu_0 \left(\nabla \times \frac{\partial \vec{H}}{\partial t} \right), \quad (2.6)$$

$$\nabla \times \nabla \times \vec{E} = -\mu \mu_0 \frac{\partial}{\partial t} (\nabla \times \vec{H})$$

$$\nabla \times \nabla \times \vec{E} = -\mu \mu_0 \frac{\partial}{\partial t} \frac{\partial \vec{D}}{\partial t}.$$

Substituting $\vec{D} = \epsilon \epsilon_0 \vec{E}$ gives

$$\nabla \times \nabla \times \vec{E} = \mu \mu_0 \epsilon \epsilon_0 \frac{\partial^2 \vec{E}}{\partial t^2}.$$

Using the vector identity

$$\nabla \times \nabla \times \vec{E} = \nabla(\nabla \cdot \vec{E}) - \nabla^2 \vec{E} \quad (2.7)$$

and assuming the homogenous medium (meaning there is no gradient in the electric susceptibility), we can say $\nabla \cdot \vec{E} = 0$

Decomposing the Laplacian operator into its components

$$\nabla^2 E = \nabla^2 E_x \hat{x} + \nabla^2 E_y \hat{y} + \nabla^2 E_z \hat{z}$$

and

$$\nabla^2 = \frac{\partial^2}{\partial x^2} + \frac{\partial^2}{\partial y^2} + \frac{\partial^2}{\partial z^2} \quad (2.8)$$

we can write two separate wave equations for electric and magnetic fields as

$$\nabla^2 \vec{E} - \mu\mu_0 \epsilon\epsilon_0 \frac{\partial^2 \vec{E}}{\partial t^2} = 0 \quad (2.9)$$

and

$$\nabla^2 \vec{H} - \mu\mu_0 \epsilon\epsilon_0 \frac{\partial^2 \vec{H}}{\partial t^2} = 0 \quad (2.10)$$

2.2 TE, TM and Quasi TE, TM modes

The electromagnetic energy in waveguide structures propagates in discrete spatial modes with discrete propagation constants. These modes exist in different



Figure 2-1. A side cross-section of a simple slab waveguide, where a higher refractive index material n_c is surrounded by two lower refractive indices of n_s .

forms and are dependent on the geometry of the waveguide. One of the geometries is a thin-film waveguide which is a 2D slab described in Figure 2-1. A higher refractive index material is sandwiched between two lower refractive index materials that form a cladding. In the case of an asymmetric waveguide the upper and lower refractive indices are of different values, whereas in a symmetric waveguide they are of same value. Such a structure is called as a planar slab waveguide. In such a planar slab waveguide the field is confined only in one dimension, and in the other two dimensions the field does not face any refractive index discontinuity and is extended to infinity. The other two dimensions are the propagation dimensions of the wave. Without the loss of generality, the orientation of the axes can be chosen so that the propagation direction is along the z -axis. Hence the equation (2.9) reduces to a one-dimensional form and is given by

$$\frac{\partial^2 E_y}{\partial x^2} + (k_0^2 n_i^2 - \beta^2) E_y = 0, \quad (2.11)$$

where the electric field is polarized along y direction and energy is propagating in z direction. After applying the boundary conditions of the tangential components of the electric and magnetic fields being continuous across the boundary, the field components in each layer are given as follows:

$$\begin{aligned} E_y(x) &= A e^{-\gamma_c x}, \quad 0 < x, \\ E_y(x) &= B \cos(k_f x) + C \sin(k_f x), \quad -h < x < 0, \\ E_y(x) &= D e^{-\gamma_s(x+h)}, \quad x < -h. \end{aligned} \quad (2.12)$$

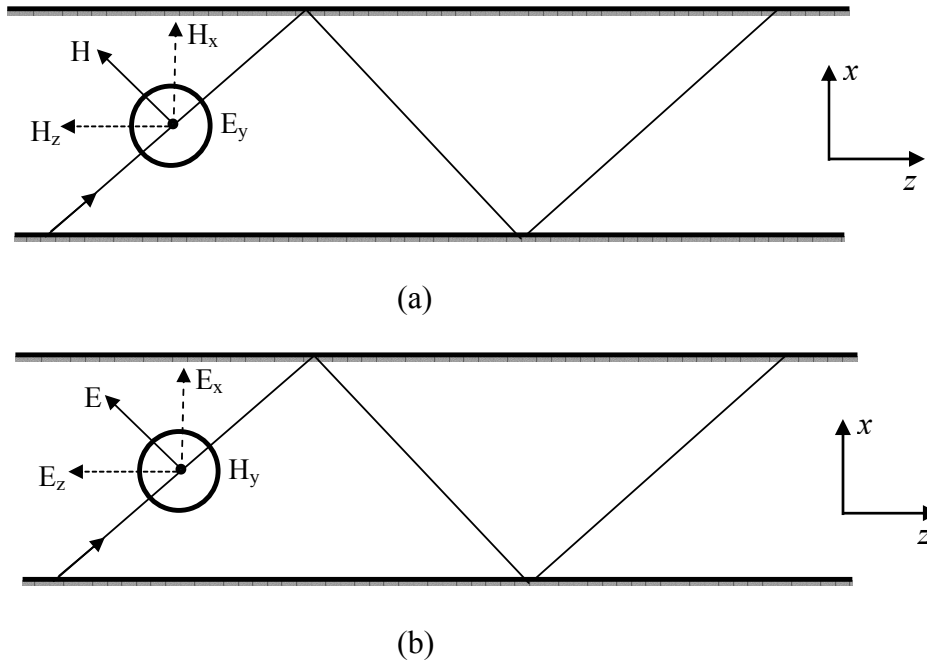


Figure 2-2. (a) A slab waveguide supporting TE mode. (b) A slab waveguide showing the propagation of a TM mode.

Here the coefficients A, B, C, D are amplitude coefficients, and k_f , γ_c , and γ_s are the transverse propagation constants in the guiding film and claddings, respectively. Since the field is confined only along x direction, is polarized in y direction, and is transverse, this forms a TE mode with magnetic field having components along 'x' and 'z' directions. The components of E_x and E_z are zero. One can find the magnetic field component along z by using

$$H_z = \frac{i}{\omega\mu\mu_0} \frac{\partial E_y}{\partial x} \quad (2.13)$$

Similarly the TM modes have components E_x, E_z, H_y . A slab waveguide can have perfect TE and TM modes.

Since the energy is propagating along z direction, the Poynting vector is given as

$$S_z = \frac{1}{2} \text{Re}[(\vec{E} \times \vec{H}) \cdot \hat{z}], \quad (2.14)$$

and the time-averaged power flow along the guiding waveguide is

$$P_z = \frac{1}{2} \int_{-\infty}^{\infty} E_y H_x dx = \left(\frac{\beta}{2\omega\mu\mu_0} \right) \int_{-\infty}^{\infty} |E_y|^2 dx . \quad (2.15)$$

If the requirement for field confinement is in two dimensions, which is needed in various applications (e.g., those involving horizontal evanescent coupling), then the field needs a refractive index discontinuity in horizontal

direction as well. Such structures form two-dimensional waveguide and are known as channel waveguides. These waveguides, instead of pure TE, TM modes, support quasi-TE and quasi-TM modes that are also denoted as E_{nm}^x and E_{nm}^y modes.

Since the field confinement is in two dimensions, the wave equation includes electric and magnetic field components varying in both dimensions. The electric field obeys the following wave equation:

$$\frac{\partial^2 \vec{E}}{\partial x^2} + \frac{\partial^2 \vec{E}}{\partial y^2} + [k_0^2 n^2(x, y) - \beta^2] \vec{E} = 0. \quad (2.16)$$

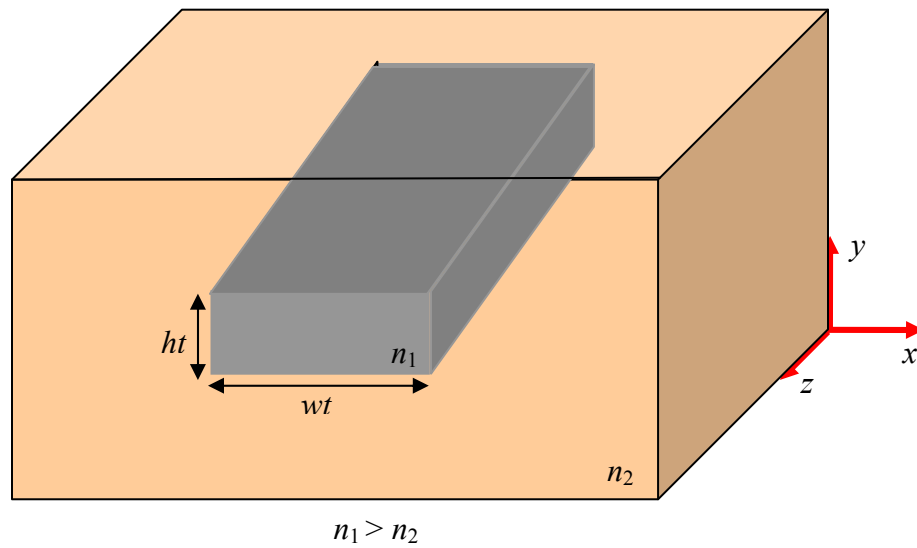


Figure 2-3. A channel waveguide with core buried in the cladding of refractive index n_2 .

Similarly to the one-dimensional case, by applying the boundary conditions of tangential components of electric and magnetic fields being continuous this time along four boundaries, the equation is solved. This is usually done numerically. The popular numerical methods of solving such an equation to find the propagating modes in the guiding structure are FDTD (Finite-Difference Time-Domain) and FD BPM (finite-difference beam-propagation method). These methods have several advantages, especially in simulating complicated geometries and when the refractive index profile is varying across the geometry. We use FD BPM from the commercially available software [52].

The schematic of the structure that is used in our case is shown in the Figure 2-3. The high-refractive-index silicon-nitride layer is surrounded by the low-index silicon dioxide. The Sellmeier equation for both silicon nitride and silicon dioxide are given as follows [53]:

$$n_{\text{SiO}_2} = \sqrt{1 + \frac{1.09877\lambda^2}{\lambda^2 - 92.4317^2}} \quad (2.17)$$

and

$$n_{\text{Si}_3\text{N}_4} = \sqrt{1 + \frac{2.8939\lambda^2}{\lambda^2 - 139.67^2}} \quad (2.18)$$

These equations are incorporated in the simulation tool, and the propagation constants are obtained by numerically solving the equation using the FD BPM software. As the dimensions become larger, these waveguide structures can support multiple modes. Our requirement for coupling the light to the microresonator involves a single-mode operation of the bus waveguide, and we determine the cutoff condition for the single-mode operation by using the Rsoft, BeamProp software module. The results of the simulation are shown in Figures 2-4 and 2-5 below. In the fabrication of such a waveguide, the horizontal dimensions can be increased up to the cutoff condition for different heights of the waveguides.

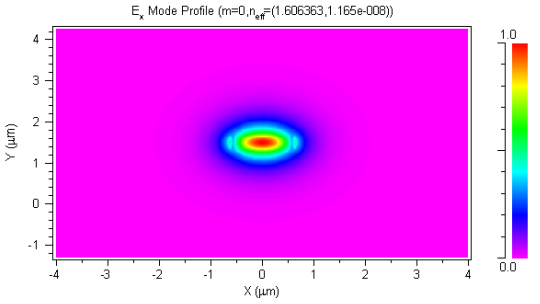
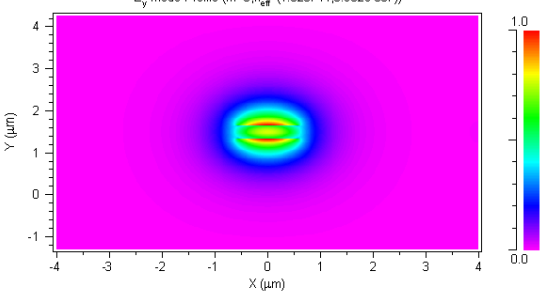
wt=1.2 ht=0.32	n_{eff}	Mode
Quasi TE	1.606363	 <p>The plot shows the E_x mode profile for a Quasi TE mode. The x and y axes range from -4 to 4 micrometers. The field is concentrated in a central region, with a color scale from 0.0 to 1.0. The profile is roughly circular with a slight horizontal elongation.</p>
Quasi TM	1.528744	 <p>The plot shows the E_y mode profile for a Quasi TM mode. The x and y axes range from -4 to 4 micrometers. The field is concentrated in a central region, with a color scale from 0.0 to 1.0. The profile is roughly circular with a slight vertical elongation.</p>

Figure 2-4. Simulated mode profiles in the channel waveguide.

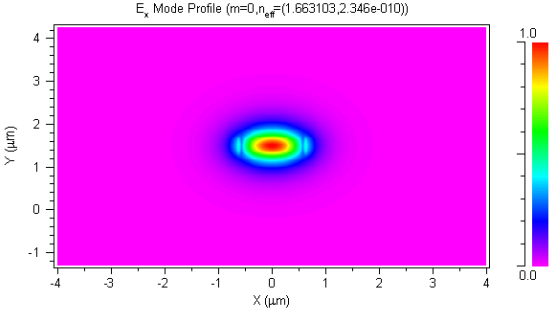
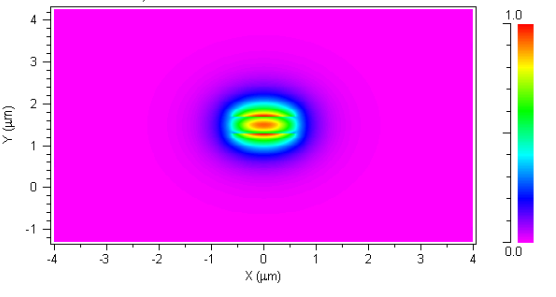
wt=1.2 ht=0.415	n_{eff}	Mode
Quasi TE	1.663103	 <p>E_x Mode Profile ($m=0, n_{\text{eff}}=(1.663103, 2.346e-010)$)</p>
Quasi TM	1.589291	 <p>E_y Mode Profile ($m=0, n_{\text{eff}}=(1.589291, 5.606e-009)$)</p>

Figure 2-5. Simulated mode profiles for a thicker core in a channel waveguide.

2.3 Microring Resonators

Microring resonators are waveguide structures monolithically fabricated typically on silicon substrates, which have potential applications as optical channel dropping filters [54–56], as higher-order filters [57, 58], and as optical delay buffers [59, 60] in telecommunications, and also as sensors [61–63].

A ring resonator is primarily a cavity system analogous to an asymmetric Fabry-Perot cavity with one side having a 100% reflector, which is also known as a Gires-Tournois interferometer. However, one of the major differences between the two is how the energy inside the cavity behaves. A Fabry-Perot system produces a standing-wave pattern, whereas in a ring resonator a traveling wave is formed, where the electromagnetic energy entering the resonator propagates inside the circular or racetrack cavity multiple times, and the energy builds up.

Geometrically, the ring resonator has an azimuthal symmetry supporting both cw & ccw waves that are degenerate, i.e., they have the same resonance frequencies. Such a ring resonator alone cannot be utilized unless there is a coupler so that the resonant cavity can be accessed, and the waveguide through which this access takes place is a bus waveguide. Electromagnetic energy flowing through the bus waveguide is coupled into the ring cavity through a “coupler”. The four-port coupler and the ring together can be treated as a lumped element [64], even though the interactions happen over a finite length.

In an ideal case a ring resonator system is an all-pass filter, i.e., it passes all signal wavelengths with the delay of the signal defined by the number of round trips taken by the coupled energy. The light propagating through the bus waveguide (straight waveguide) and having the wavelength satisfying the resonance condition $m\lambda=2\pi Rn_{\text{eff}}$ enters the ring resonator with a coupling coefficient of τ and, after circulating in the ring the number of times determined by the finesse of the cavity, exits the ring into the bus waveguide.

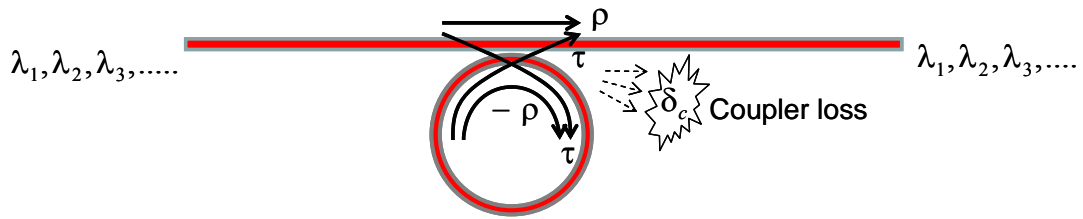


Figure 2-6. Cartoon showing the microring resonator with coupling coefficient τ and the reflection coefficient ρ .

The light output is the light reflected from the cavity into the bus waveguide. If there is loss δ_c during the coupling of the light between the ring cavity and the straight waveguide, then all the coefficients satisfy the following condition in accordance with the conservation of energy:

$$\tau^2 + \rho^2 = 1 - \delta_c \quad (2.19)$$

In the steady-state analysis, the electric field after one round-trip can be expressed as

$$\begin{aligned}
E_1 &= E_0 e^{ik_{\text{eff}} \cdot 2\pi R} e^{-(\alpha \cdot 2\pi R)/2} \\
&= E_0 e^{i\varphi_0} e^{-\delta_p/2} \quad ,
\end{aligned} \tag{2.20}$$

where δ_p is the round-trip loss coefficient. Then the output field is the summation of the phasors representing the fields after each round-trip, which can be expressed as [65]:

$$\begin{aligned}
E_{\text{out}} &= E_{\text{in}} \{ \rho + \tau^2 [e^{i\varphi_0} e^{-\delta_p/2} [1 + (-\rho e^{i\varphi_0} e^{-\delta_p/2}) + (-e^{i\varphi_0} e^{-\delta_p/2})^2 + \dots]] \} \\
&= E_{\text{in}} \left\{ \rho + \frac{\tau^2 e^{i\varphi_0} e^{-\delta_p/2}}{1 + \rho e^{i\varphi_0} e^{-\delta_p/2}} \right\} , \\
E_{\text{out}} &= E_{\text{in}} \frac{\rho + (\rho^2 + \tau^2) e^{i\varphi_0} e^{-\delta_p/2}}{1 + \rho e^{i\varphi_0} e^{-\delta_p/2}} = E_{\text{in}} \frac{\rho + (1 - \delta_c) e^{i\varphi_0} e^{-\delta_p/2}}{1 + \rho e^{i\varphi_0} e^{-\delta_p/2}} ,
\end{aligned} \tag{2.21}$$

$$\begin{aligned}
P_{\text{out}} &= P_{\text{in}} \left| \frac{\rho + (1 - \delta_c) e^{i\varphi_0} e^{-\delta_p/2}}{1 + \rho e^{i\varphi_0} e^{-\delta_p/2}} \right|^2 \\
&= P_{\text{in}} \frac{\rho^2 + (1 - \delta_c)^2 e^{-\delta_p} + 2\rho(1 - \delta_c) e^{-\delta_p/2} \cos \varphi_0}{1 + \rho^2 e^{-\delta_p} + 2\rho e^{-\delta_p/2} \cos \varphi_0} .
\end{aligned} \tag{2.22}$$

If there is loss in the ring cavity, then one can see the resonances as dips in the power level at periodic frequency spacings.

2.4 Operating regimes of resonators

The gap between the bus waveguide and microring is also critical in determining the operation range and the losses of the resonator. If the gap

between the two becomes zero then there will be a significant loss because of mode mismatch in the coupling region [66]. Avoiding this loss involves the design of an adiabatic coupler which includes more complications in the design and fabrication also. Hence a fixed gap (not zero) has to be used.

As discussed above, the energy is coupled into the ring resonator through a bus waveguide by a four-port coupler. The parameters of the reflection coefficient, losses in the ring cavity, and losses in the coupler determine the resonance widths and the transmitted power from the output port. The magnitudes of these coefficients determine the operating regime of the ring resonator. There are three different operating modes of the ring resonator. They are

1. Critically-coupled,
2. Under-coupled,
3. Over-coupled.

The coupler parameters are defined as follows:

$\kappa = \tau^2 \rightarrow$ Power coupling coefficient,

$\delta_p \rightarrow$ Loss coefficient in the ring,

$\delta_c \rightarrow$ Loss coefficient of the coupler.

Critically-coupled condition:

Critically-coupled ring resonator has zero reflections from the ring at the resonance frequencies. This is akin to impedance matching in a network. This can also be expressed as a complete destructive interference between the transmitted field and the field reflected back by the ring. All the power in the resonator is lost in the cavity because of the loss, and no light comes out. The coupling coefficient in this regime is exactly equal to the losses:

$$\kappa = \delta_p + \delta_c . \quad (2.23)$$

In Figure 2-7 it can be seen that the normalized output transmission value goes to zero in the critically coupled regime of the resonator.

Over-coupled condition:

In this regime the coupling coefficient is greater than all losses combined:

$$\kappa > \delta_p + \delta_c . \quad (2.24)$$

The entering electromagnetic energy makes fewer turns inside the resonator and comes out through the coupler. The full width at half minimum of the resonance can be seen to be wider in the Figure 2-7 and thus the quality factor of such a resonator would be lower.

Under-coupled condition:

In the under-coupled condition the coupling coefficient is lower than all the losses combined:

$$\kappa < \delta_p + \delta_c. \quad (2.25)$$

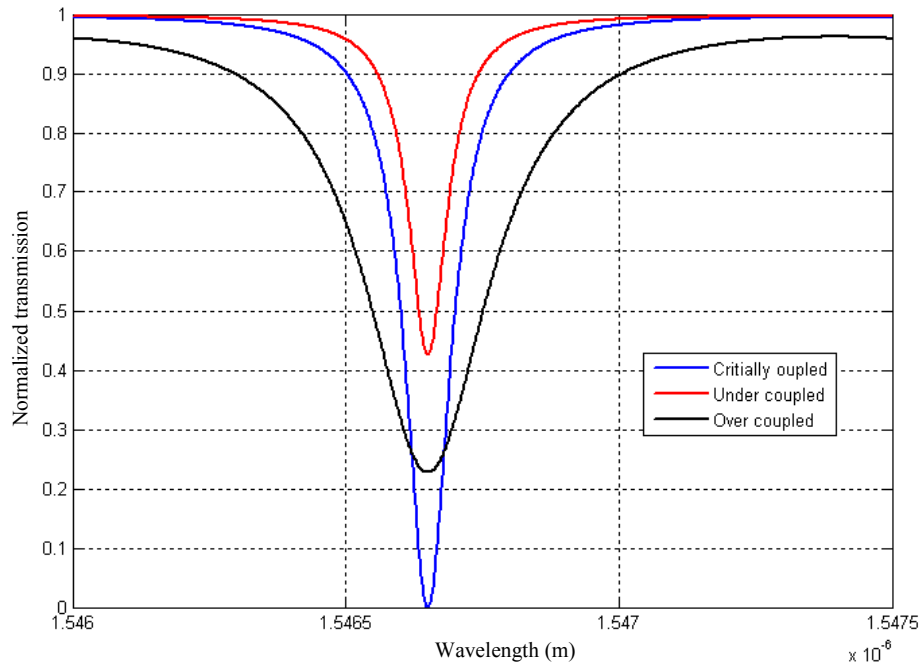


Figure 2-7. Plot showing the resonator in different operating regimes.

2.5 Parameters characterizing the ring resonators

The ring resonators are characterized by several parameters that define the different modes that resonate in the cavity, spacing between the modes and the energy stored in the cavity. The free spectral range (FSR), defined as the spacing between the modes, is given in terms of wavelength separation as

$$\Delta\lambda_{\text{FSR}} = \frac{\lambda^2}{n_g L}, \quad (2.26)$$

where n_g is the group index of the waveguide given by

$$n_g = n_{\text{eff}} - \lambda \frac{dn_{\text{eff}}}{d\lambda}. \quad (2.27)$$

The group index could be even greater than the refractive index of the core of the waveguide. It depends on whether the slope $\frac{dn_{\text{eff}}}{d\lambda}$ is positive or negative. The

finesse F of the resonator is given by

$$F = \frac{\text{FSR}}{\text{FWHM}}, \quad (2.28)$$

where FWHM (full width at half minimum) is the width of the resonance at a level 3 dB below the maximum transmission value of the resonator. The finesse determines the number of round trips the field coupled into the ring makes. The quality factor of the resonator is defined as ratio of the amount of energy stored in the resonator to the energy lost per cycle and is given by

$$Q = \frac{\lambda}{\Delta\lambda_{\text{FWHM}}}, \quad (2.29)$$

where $\Delta\lambda_{\text{FWHM}}$ is the full width at half minimum of the resonance, and λ is the central wavelength of the resonance.

2.6 Summary

In this chapter a theoretical introduction to optical waveguides has been presented. We have discussed the optical waveguides designed for single-mode operation at wavelength 1550 nm and extracted the effective refractive indices from the simulation. The microring resonator theory, different modes of the operation of the resonator with respect to the coupling coefficient, and the important parameters that characterize the performance of microring resonators have been also presented.

CHAPTER 3

FABRICATION AND CHARACTERIZATION OF MICRORINGS

The fabrication of low-loss photonic waveguides involves several CMOS processing tools and has stringent requirements. The scattering of the electromagnetic energy because of the sidewall roughness in the waveguides contributes to a significant loss of optical power in the waveguides. In particular, when the waveguide dimensions become nearly equal to the wavelength of operation, a significant part of the mode extends into the cladding, and the roughness at the interface between the core and the cladding becomes an important factor. Hence, extreme care has to be taken during the fabrication process to optimize each process step to minimize the sidewall roughness in the waveguides.

In the fabrication, a *p*-type 4" Si wafer is taken and is cleaned in a piranha solution, which is a combination of H₂SO₄ and H₂O₂ in a 3:1 ratio. This solution strongly removes the organic impurities, if any are present on the surface. A set of six such wafers were used and all underwent the same cleaning process. These wafers were then oxidized to grow a 3.5- μm -thick SiO₂. A 900-nm-thick oxide was first grown by dry oxidation without using water vapor in the furnace, which gives a very high quality surface, and the remaining 2.6 μm was grown by wet oxidation process.

A stoichiometric silicon nitride layer of thickness 320 nm is deposited on these wafers by LPCVD process. Silicon nitride (SiN) can also be deposited by PECVD process, but the quality of the film in terms of uniformity is not comparable to LPCVD process. The low pressure in the LPCVD enables the flow of the reactant mass on to the surface of the wafer to react and is significantly slower, which enables a very high densification of the deposited film with extremely low defects.

The cleaned wafers are introduced into the furnace and a gas mixture of dichlorosilane (DCS) at a flow rate of 25 sccm and ammonia NH₃ at a flow rate of 75 sccm is used. The furnace is maintained at a pressure of 250 mT and the deposition happens at a temperature of 770°C. The following chemical equation describes the deposition process:



Silicon nitride films develop high tensile stress on the orders of GPa (Giga Pascal) [67, 68], and hence instead of depositing in one step, a two-step deposition is done to reduce the problem of film cracking. This deposition was done in two steps of 150 nm and 170 nm separately. After the first deposition step the wafers were cooled down to room temperature, and after that the deposition is continued. This ensures that the tensile stress of the silicon nitride film does not result in the

film cracking during the deposition process, even though for very thick films the tensile stress poses a significant problem. The deposition of the films was done at a rate of 25 Å/min and a bare silicon wafer was used in this process along with the wafers with oxide film to monitor the thickness of the film deposited. In this process, a variation of 20 nm of film thickness was observed, depending upon the position of the wafer in the furnace, and each wafer had an excellent film uniformity which was measured by a 5 point method.

After LPCVD deposition the wafers were diced into 10 mm × 10 mm pieces by a dicing machine, and the diced pieces were used in the further processing steps.

3.1. E-beam lithography process

The waveguides and microrings are patterned using the electron beam lithography process which is called as E-beam lithography. Unlike photolithography, where a wide beam of light falls onto a photo mask, and underneath exists a polymer-coated (photoresist) sample, in the e-beam lithography process, a direct beam of electrons strike the surface of the resist sensitive to electron charge. Thus, this is a direct writing process. Instead of a physical photomask, a CAD file loaded into the computer operating the electron beam machine includes the pattern. The theoretical resolution capability is determined by the diffractive limit of the source and the de Broglie wavelength of a 30-kV e-beam gun used in this

experiment, and yields a value about 7 pm. But eventually the resolution of the pattern is determined by the resist that is used in this experiment. The best resolution of the resist used in this experiment is 50 nm.

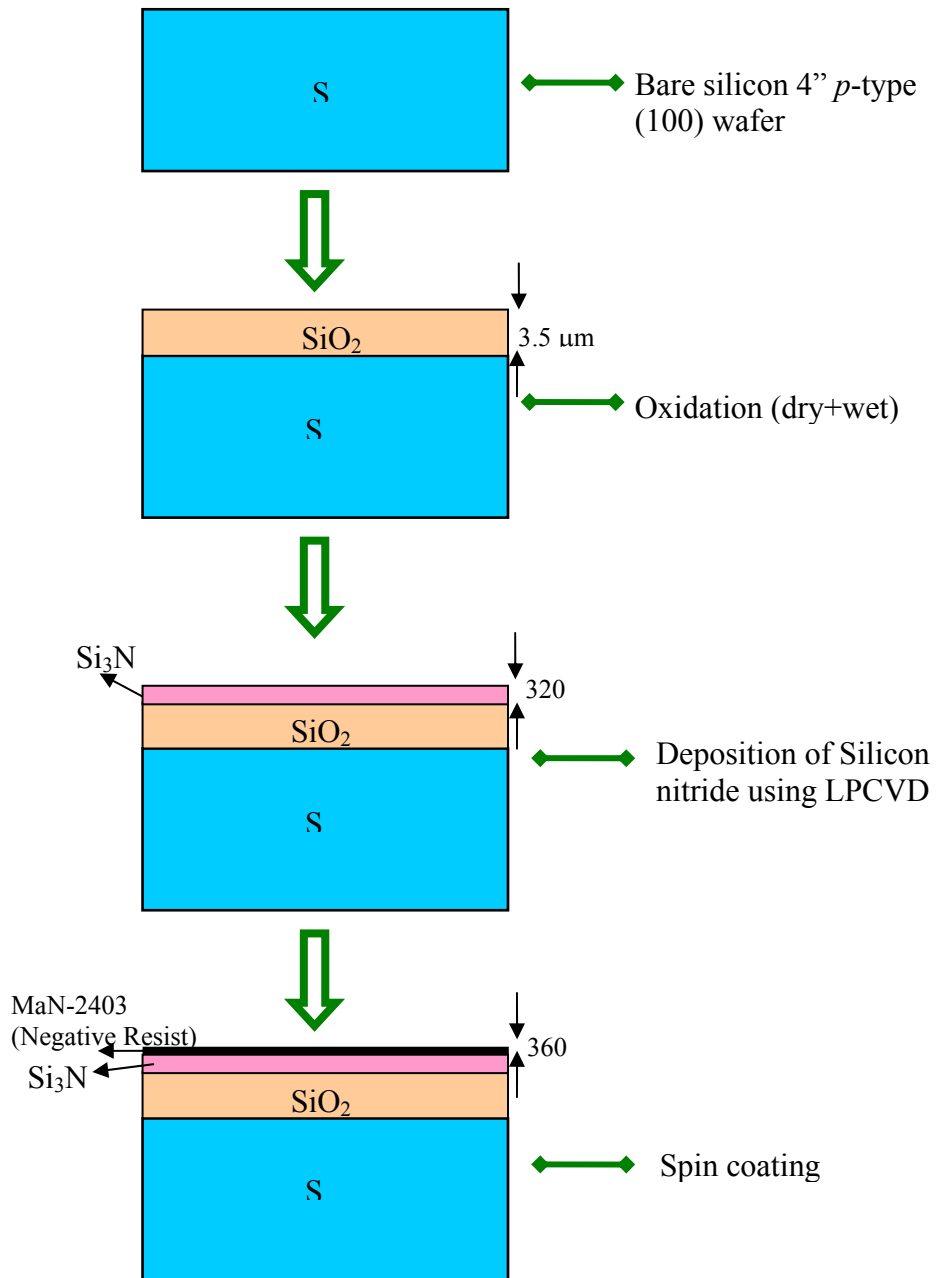
The samples used for e-beam lithography are perfectly cleaned by ultrasonically agitating for 5 min in acetone followed by a 2-min agitation in methanol. After that a 10-min ultrasonic agitation in DI (deionized) water is also done, and the samples are tested under optical microscope for any contamination, because during the dicing of the samples the dirt particles could have attached themselves to the surface of the samples.

Once the sample surfaces are ultra clean, they are baked at a temperature 150° C for 20 min, so that all the moisture gets evaporated. After that the samples are taken out from the baking plate and cooled for 5 minutes. Then a negative e-beam resist MaN-2403 is spin coated at 2000 rpm. The sample is subsequently soft-baked at 95°C for 2 min. After that the sample is taken to the e-beam lithography process.

The design work of the waveguides and microrings is done on Design CAD software associated with NPGS (nanopattern generation software) of the e-beam lithography system. Several parameters effect the quality of the pattern formed on the resist. The acceleration voltage is set at 30 kV, which is the maximum available voltage. The higher the acceleration voltage, the better is the control of the horizontal dimension of the pattern formed. Lower acceleration

voltages are prone to exposing unwanted areas due to the proximity effects. The electrons possess lower kinetic energy in the lower acceleration voltage columns, and they do not penetrate deep enough in the resist, scatter back on the surface, and expose the unwanted areas surrounding the desired pattern.

In the fabrication of microring resonator the length of the waveguide was 5 mm, which is beyond the minimum allowed magnification ($\times 97$) at a 6 mm working distance in the machine. Still, the pattern can be written without stitching errors. The e-beam dose (charge density), used in this case, was $120 \mu\text{C}/\text{cm}^2$. But when the curved waveguides were being written during the fabrication of AMZI (asymmetric Mach-Zehnder interferometer) couplers (discussed in chapter 4) with microrings, where a thicker e-beam resist Ma-N 2405 was used, stitching errors were significantly pronounced and the length of these waveguides had to be reduced to a value within the allowed least magnification of the system. The AMZI waveguide was written at a magnification of $\times 118$, and the dosage used was $220 \mu\text{C}/\text{cm}^2$. The length of these waveguides was 3 mm. In these patterns the stitching errors were found to be reduced by selecting “multipath” mode in the NPGS software settings whose value was set to be 5. This basically divides the dosage by a magnitude set in this option field and repeats the pattern 5 times. The beam current used in this process was between 30 pA and 40 pA and was changing from day to day. The lower the beam current, the more time it takes to write the pattern. The process flow is shown in Figure 3.1.



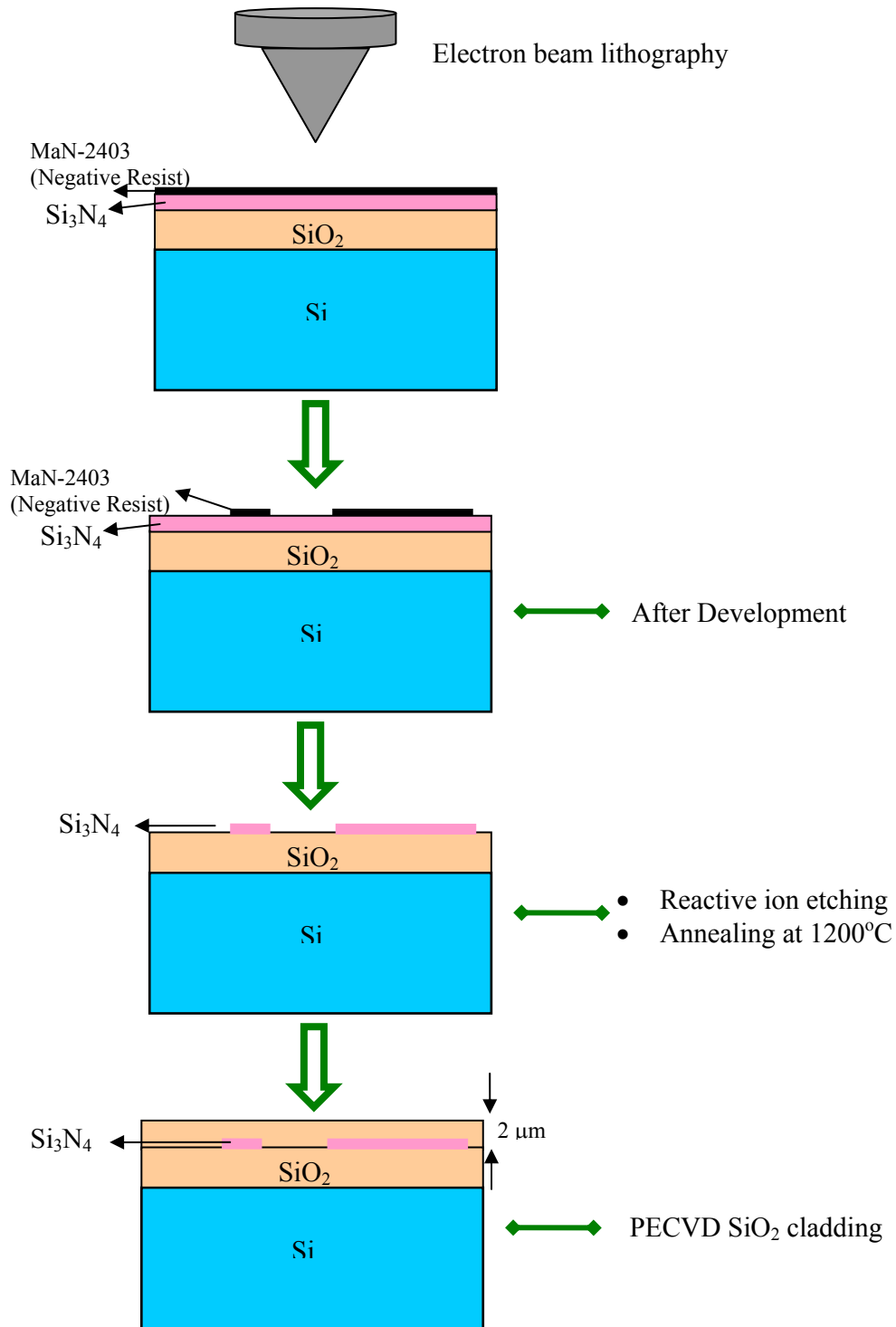
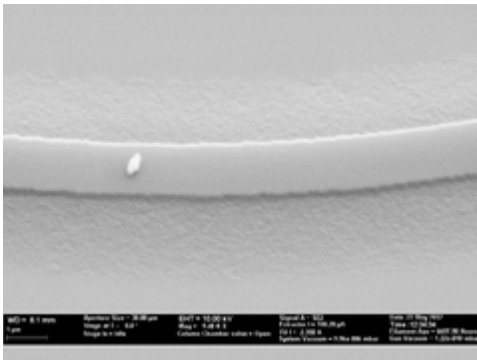


Figure 3-1. Fabrication process flow.

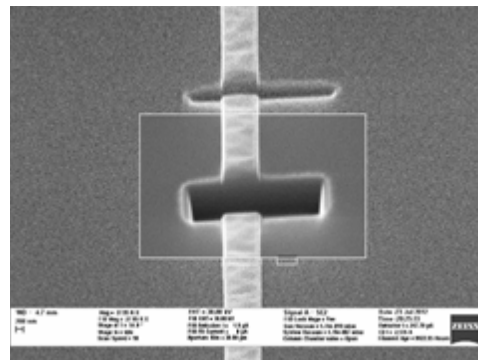
Once the patterns have been defined, the sample is developed in the developer MaD-525 without post-exposure bake in this resist. This process is done very carefully in two steps. First, the sample is carefully placed inside the developer solution, and the beaker is mildly agitated for every 5 seconds; this is done for 1 minute. Once this has been done for 60 seconds, the beaker is placed in an ultrasonic bath and agitated ultrasonically for 30 seconds. This step is very important, because during the e-beam lithography process the narrow gap (400 nm) between the waveguide and the microring is also exposed by the e-beam owing to the proximity effects discussed above, and the gap remains not fully open. The resist existing in this gap needs to be removed, and the two-step process significantly opens the gap. But if the gap is not completely opened, then there would be a loss in the coupler, which diminishes the performance of the microring cavity. Since the beam current was changing from day to day, it affected the development time significantly, even though the dosage for the exposure remained same. Hence, if the gap opening was not proper for the time mentioned above, it was optimized by a few more seconds with all other conditions remaining same.

Once this has been done, if there still exists undeveloped resist in the gap between the waveguides and surroundings, the sample is developed in an oxygen plasma atmosphere. This step is done before the etch step begins, and is carried out in the TRION DRIE chamber using only lower electrode with 100 W of

power, 30 mT of chamber pressure, 50 sccm flow rate of helium and 5 sccm flow rate of oxygen for 30 seconds. This step will etch the e-beam resist and decrease the thickness of it at 3 nm/sec also. So the time was carefully chosen to avoid excess loss of resist, since the selectivity of the resist to the etching of the nitride was nearly equal to 1:1.25. But this still leaves the edges of the pattern appearing like “mouse bites” (rough), which can be confirmed by taking the SEM image of the developed pattern as shown in Figure 3-2. If this is directly etched, then this same roughness would be transferred to the actual layer. Hence this sample was baked at 145°C for 5 minutes, which contributes to reflow of the resist and makes the edges of the resist extremely smooth [69].



(a)



(b)

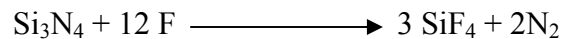
Figure 3-2. SEM images of a part of the pattern before etching. (a) Without baking the resist. (b) Cross-section after baking the resist to reflow. Image was taken after FIB milling of the cross-section.

3.2. Reactive Ion Etching

The pattern transfer was done using TRION DRIE (Deep reactive ion etching) tool, even though the etch depth in two cases was 320 nm and 415 nm, which are not very deep. This tool is equipped with inductively coupled plasma top electrode, which is very important in raising the density of the free radicals. In reactive ion etching the accelerated electrons in the plasma create free radicals, which are the unstable reactive species, and these free radicals react with the material being etched. The etching gas used was CHF₃, which etches the silicon nitride with smooth sidewalls. The following chemical equation describes the reaction happening during the process [70-72]:



The unstable fluorine reacts with the silicon nitride during the etching process:



During the etching process a fluorocarbon film is deposited on both the side walls and on the surface and, if CHF₃ alone is used, the etch rate comes to zero after

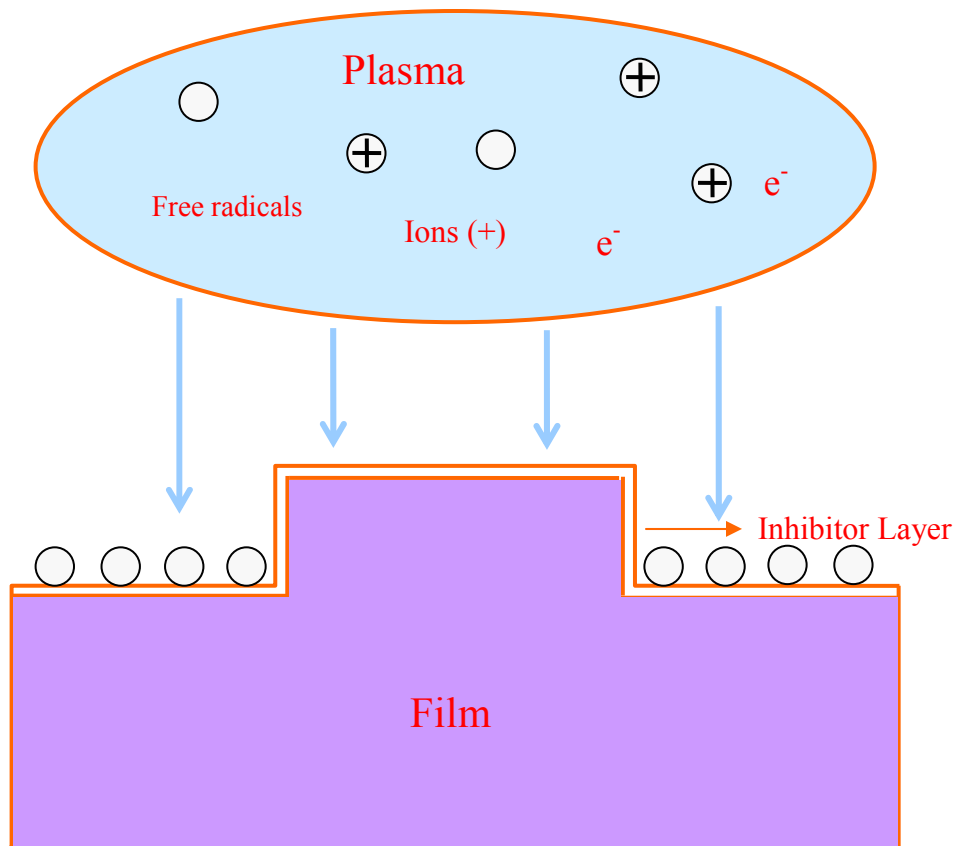


Figure 3-3. Process of reactive ion etching.

few tens of seconds before complete etching is done. Hence a small amount of O_2 is also introduced, which helps in inhibiting the formation of fluorocarbon film as it reacts with carbon to form CO_2 or CO . Care was taken to not include too much oxygen during the process, because it would etch away the e-beam resist. A 2 sccm flow of oxygen was continuously used throughout the etch process. Also a 20 sccm flow of helium was constantly used to maintain good plasma inside the chamber. Figure 3-3 depicts the reaction process.

The energy of the ions which enable the reactionary process on the surface of the film is also very important. If the energy of ions is too high, then they collide with each other and produce uneven incidence on the sidewalls, resulting in sidewall roughness. Thus the lower electrode was optimized to the RF power of 15 W in this case, and the energy of the ions would be lower, ensuring the etching is smooth, which results in the sidewalls being smooth. Along with the availability of higher density of free radicals because of the upper electrode, the entire process ensures supply of reactants and the combination ensures a low energetic ions with fast etching.

Following Table 3-1 shows the parameters used for the etching process.

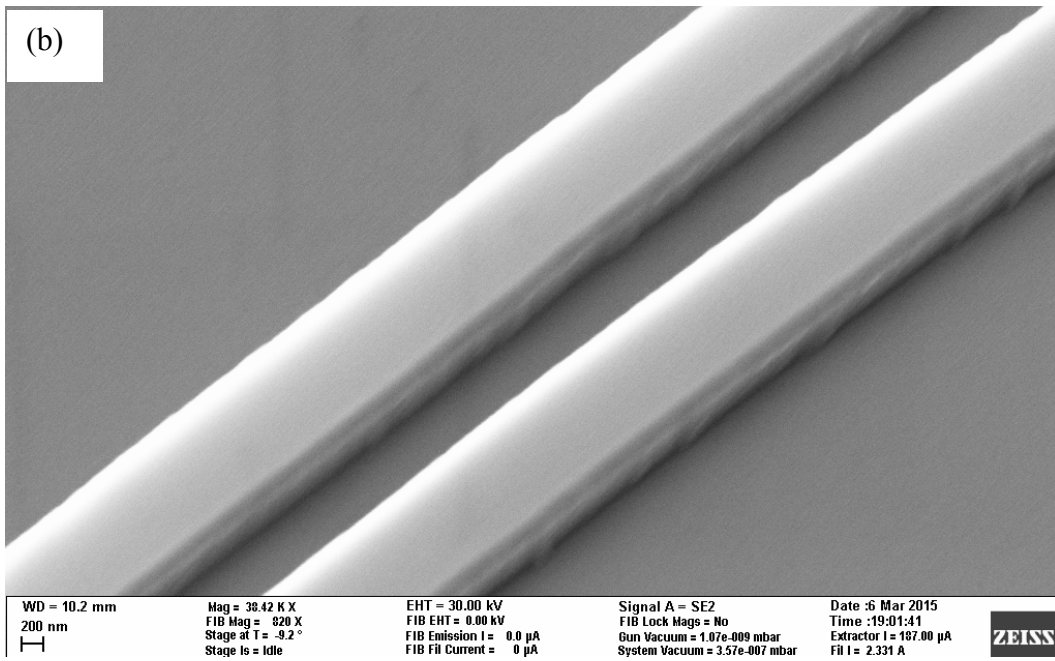
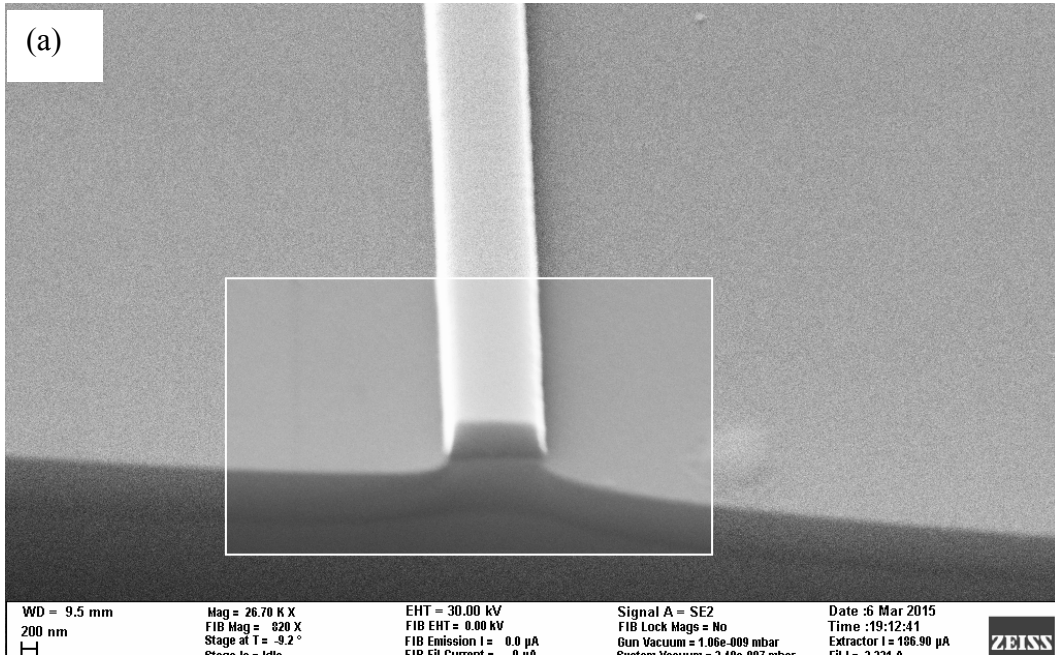
Upper electrode	2000 W
Lower electrode	15 W
Chamber pressure set	1 mT
CHF ₃	21sccm
O ₂	2 sccm
He	20 sccm

Table 3-1. TRION DRIE process parameters.

The etch rate of the silicon nitride with this recipe was 480Å/min, and this was confirmed by both profilometer- and a reflectometer-based measurements.

Once the sample had been etched, the remaining resist was stripped away in an oxygen plasma asher and by ultrasonic agitation in acetone.

The etched sample was cleaved so that the two facets of the waveguides were exposed for coupling light in and out of the waveguide. Silicon nitride has absorption peaks due to dangling N-H bonds in the material [73-76]. The absorption is in the communication band, falling in the 1550 nm wavelength region of light. Hence the waveguides are annealed in a high temperature furnace to reduce the N-H bonds so that hydrogen escapes during the annealing process. The samples are put in a furnace after making sure that they do not have any organic contamination and are annealed at 1200°C for 3 hours in a nitrogen atmosphere. The annealed samples are covered with a 2 μm of PECVD SiO_2 , which forms the upper cladding for the waveguides and microrings. The following figures show the SEM images of the fabricated waveguides and microring resonators.



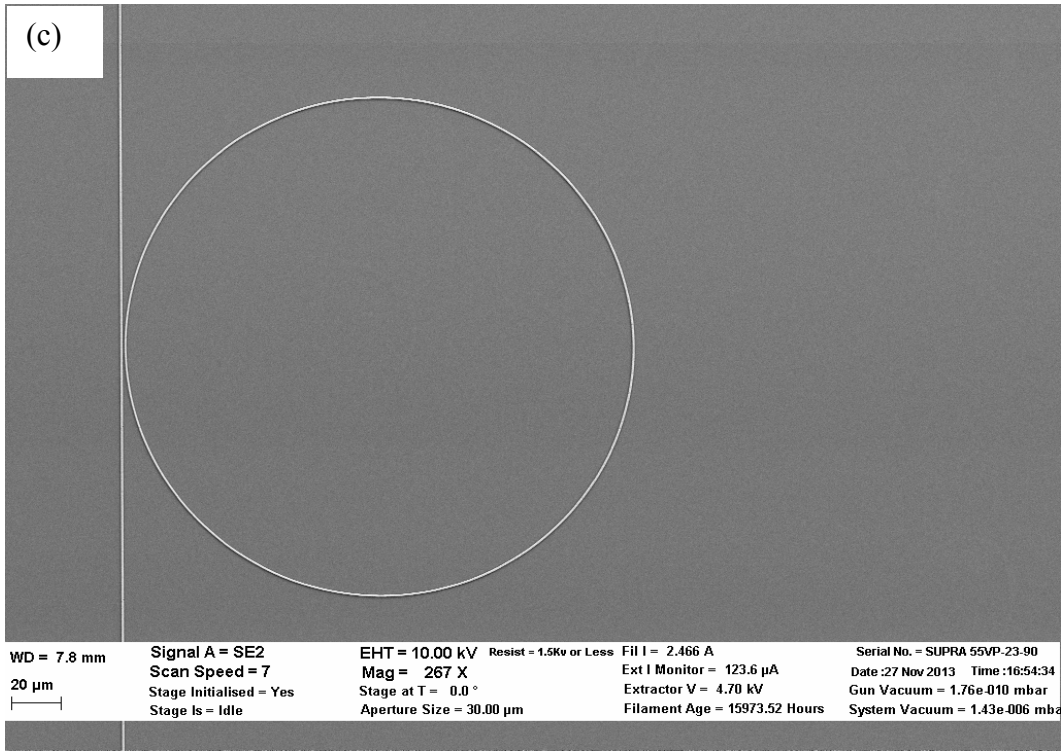


Figure 3-4. SEM micrographs. (a) Waveguide cross-section. (b) Gap between the microring and the bus waveguide. (c) Microring resonator.

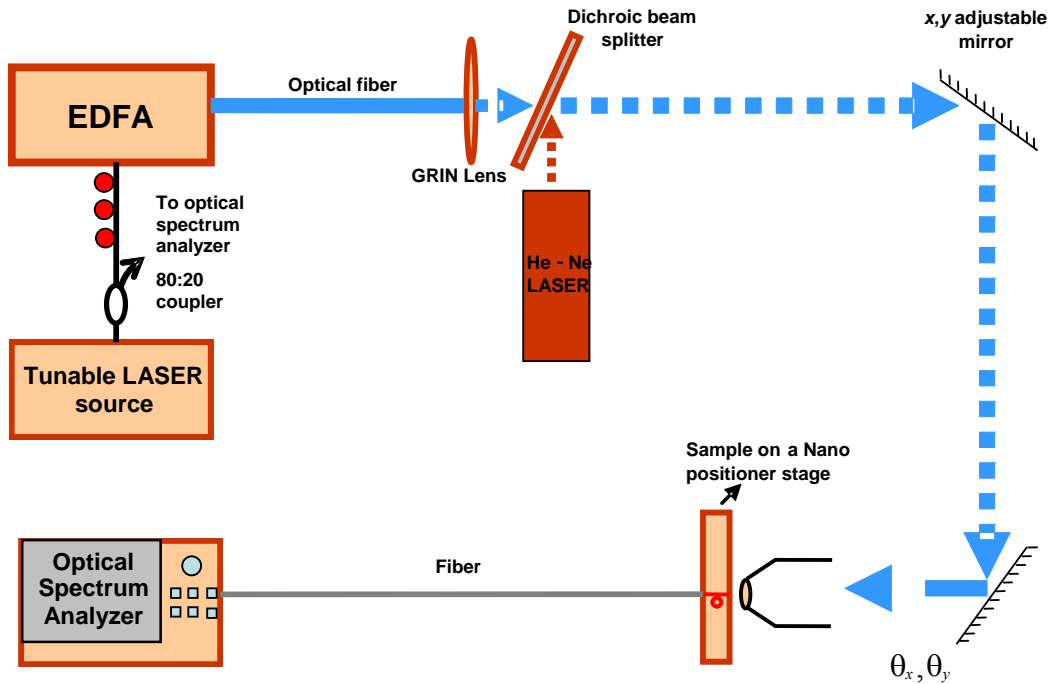


Figure 3-5. Schematic of the characterization setup.

3.3. Characterization setup

The fabricated samples are characterized for their transmission properties in a highly precise setup for coupling light into the nanoscale waveguide. The schematic of the setup is shown in Figure 3-5.

The sample is placed on an aluminum bar which is attached to a 3-axis piezo-controlled nanopositioner stage. A tunable laser source (TLS, ANDO AQ 4320) is used as the laser source. Amplified spontaneous emission from an EDFA (erbium-doped fiber amplifier) is also used to characterize a large wavelength

span including both C and L bands. A He-Ne laser is used to facilitate the coupling into the waveguide. The light from this laser is reflected by a dichroic beam splitter through which 1550 nm signal is transmitted. The signal from the tunable laser source is fed by an optical fiber to free-space collimating lens preceded by a fiber optic polarization controller. The beam of 1550 nm is aligned with the He-Ne laser and both co-propagating beams are reflected by two mirrors forming a periscopic arrangement. These beams are aligned with the axis of a 0.95 NA microscope objective. A beam expander is also made by two lenses to convert the incoming beam of diameter 1.5 μm to a 6 mm diameter, so that the spot size of the beam after the microscope objective is reduced, and coupling of optical power into the waveguide is enhanced. A polarizer is also used with its pass axis aligned to transmit '*p*' polarization to excite quasi TE mode in the waveguide. Initially, the output from the sample is coupled into another microscope objective, and the shape of the mode coming out of the sample is imaged onto an infrared detector. Then an SMF-28 fiber is butt coupled to the waveguide, and the output is connected to an optical spectrum analyzer.

3.4. Experimental Results

The transmission properties of the fabricated microring resonator are characterized using the optical spectrum analyzer with a high sensitivity and 0.01

nm resolution for the accurate measurement of the resonances. Figure 3-6 shows the characterization result of the fabricated microring resonator. The microring with 90- μm radius shows a free spectral range of 2.15 nm and the FWHM of 80 pm.

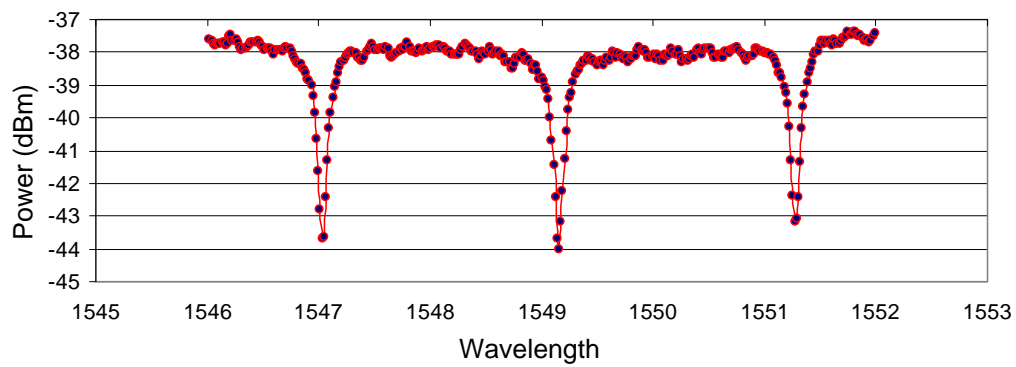


Figure 3-6. Free spectral range plot of the microring resonator with FSR value 2.15 nm.

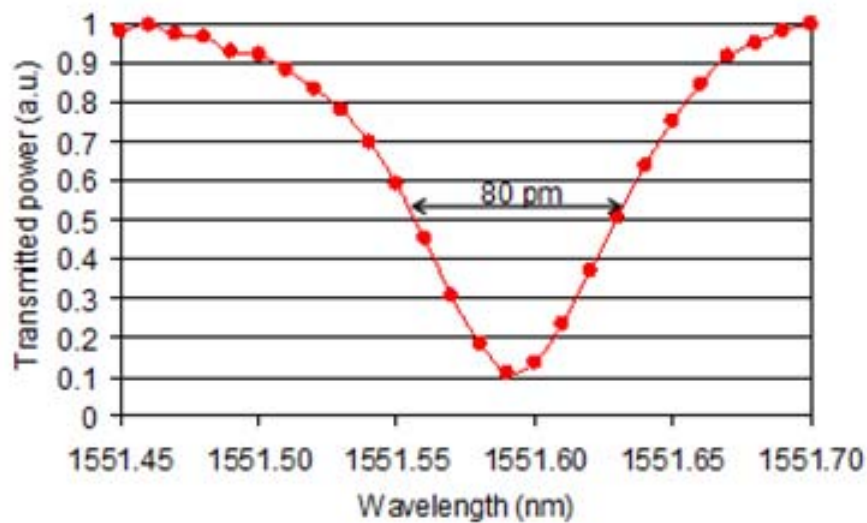


Figure 3-7. Full-width at half-minimum of 80 pm of one of the resonances.

The data from the fabricated microring resonator was analyzed and fit to the theoretical model, from which the propagation loss, coupler loss, coupling coefficient, and the operating regime of the resonator were subsequently extracted. In order to measure the propagation loss of the waveguides, the usual methodology is to employ cutback method, where waveguides of different lengths are fabricated and the ratio of the power input to the waveguide and the power collected at the output are measured and compared under similar conditions. This method intrinsically suffers from uncertainties in the coupling of input and output powers due to reasons such as the variation in the polishing quality from sample to sample [77]. This method is especially difficult for measuring losses in very low propagation loss waveguides, which requires large variation in lengths among

waveguides under comparison, and when e-beam lithography is employed to define the patterns, fabrication of long waveguides without stitching errors is a significant challenge. Hence, in this experiment the losses of the ring waveguides are estimated by fitting the resonance shapes to the propagation loss coefficients in the model. The extracted loss in the fabricated ring waveguide is 0.4 dB/mm, with a quality factor of the resonator to be 2×10^4 , and the finesse estimated to be 26 from the experimental data. By fitting the parameters we found that:

$$\delta_p = 0.066, \delta_c \ll \delta_p$$

and

$$\kappa = \tau^2 = 15.5 \%$$

The coupling coefficient in this microring resonator is greater than all the losses combined and thus this falls in the over-coupled regime. Microresonators on a substrate of thicker oxide (5 μm) layers with 0.415 nm core thickness have also been fabricated and shown an intrinsic quality factor of $\sim 8 \times 10^4$. Figures 3-8 and 3-9 show critically-coupled and under-coupled resonances of these microresonators, respectively.

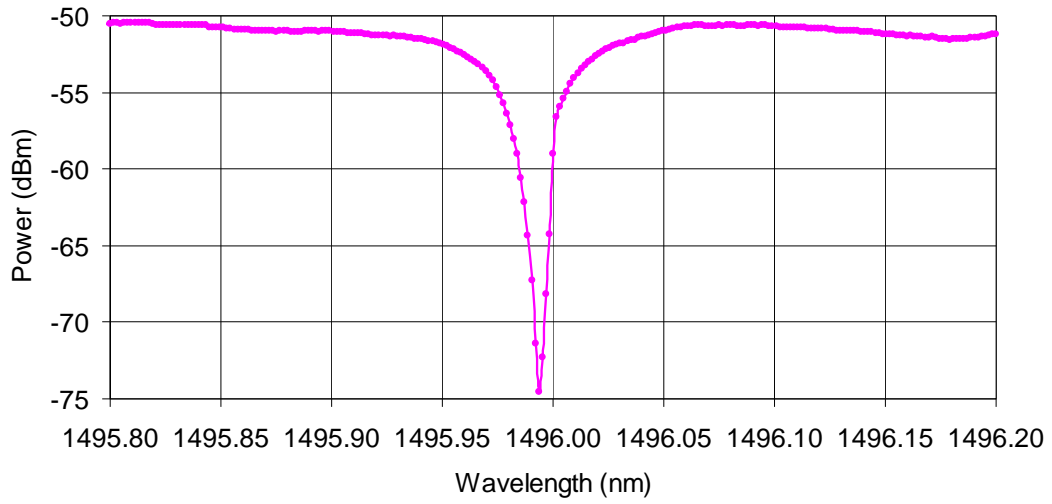


Figure 3-8. Experimental data for a critically-coupled microring resonator.

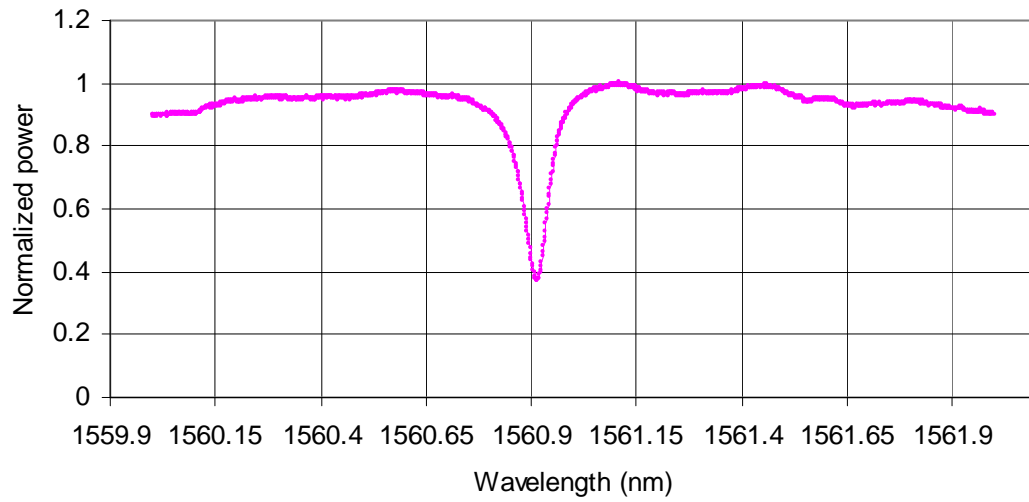


Figure 3-9. Experimental data of a microring resonator in an under-coupled regime.

3.5. Characterization of the delay line properties of microrings

A pulse entering a resonator dwells inside certain amount of time based upon the lifetime of the resonator, and the cavity hence acts as a delay line. Such phenomenon is useful in synthesizing dispersion compensators with periodic group-delay response out of multiple cascaded microrings. The delay line properties of a microresonator are experimentally investigated and are in agreement with the estimated finesse of the resonator.

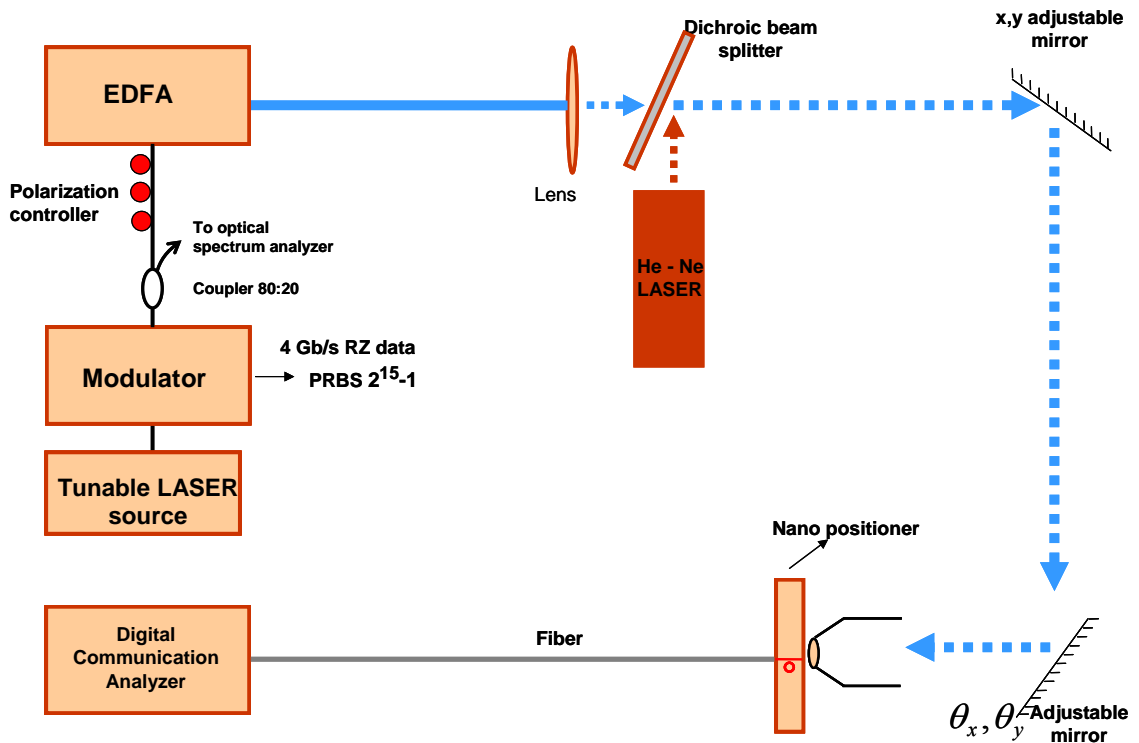


Figure 3-10. Experimental setup for investigating delay line properties of a microring.

Figure 3-10 shows the characterization setup, which is similar to that shown in Figure 3.5, but the source is a 4-Gb/s RZ-modulated data stream of $2^{15}-1$ pseudo random bit sequence produced by an electro-optic modulator. The carrier wavelength was initially positioned between the resonances, and the temporal position and shape of the pulse was recorded by a digital communication analyzer. This pulse was used as a reference. Then the wavelength of the laser was shifted to one of the resonances and the temporal position of the pulse was monitored. The pulse in this case was shown to be delayed by 14 ps indicating 4 round trips in the ring, which is in agreement with the calculation of the finesse.

The number of round trips is given as follows:

$$N = \frac{F}{2\pi}.$$

The experimental results of the pulse temporal positions are shown in the Figures 3-11.

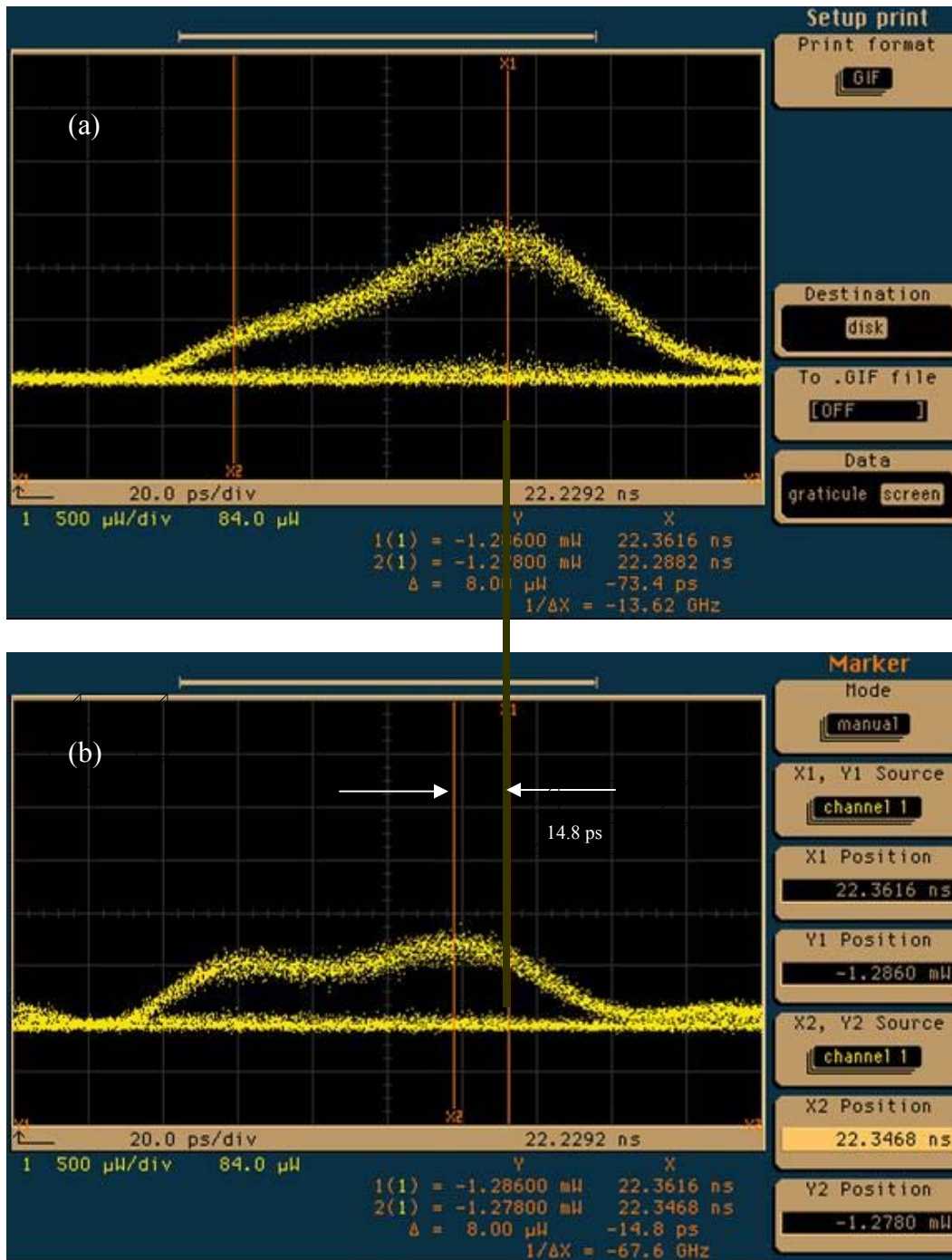


Figure 3-11. (a) Pulse positions OFF resonance. (b) Pulse position ON resonance.

3.6. Summary

In this chapter the details of the fabrication process of the microring resonators have been discussed. The optimization of process parameters at each fabrication step has been presented. The fabricated devices have been characterized, and the highest quality factor has amounted to 8×10^4 . In addition, the experimental results of the delay line properties of a microring resonator have been presented, showing that a resonant RZ pulse has been delayed by 14.8 ps by a cavity of finesse 26.8 with respect to an off-resonant pulse, which agreed with the theoretical calculation.

CHAPTER 4
ASYMMETRIC MACH-ZEHNDER INTERFEROMETER BASED
MICRORING RESONATOR

The integrated-optical microresonators have several potential applications in nonlinear-optical signal processing, especially in the generation of optical combs and in the creation of wavelength-division-multiplexed quantum states. Both of these applications rely on optical parametric gain, which is highly dependent on the chromatic dispersion experienced by the modes of the microresonator. For generation of the broadest comb and photon-pair spectra, this dispersion must be close to zero (or slightly anomalous) – this would ensure equal mode spacing in frequency, maximizing the nonlinear interaction. However, for many microresonator materials, such as silicon nitride, this requirement is not easy to satisfy. Achieving near-zero dispersion requires growing very thick silicon nitride films [78, 79], which is very challenging technologically owing to the film’s intrinsic mechanical stress.

However, there is an alternative approach, in which the mode’s group velocity dispersion is compensated by an intra-cavity dispersive element, which results in the control of the effective group index of the microresonator and equalizes the frequency spacings of its longitudinal modes. As a specific dispersive element, we consider in detail the input-output coupler based on an

asymmetric Mach-Zehnder interferometer (AMZI). The AMZIs have previously been employed for tuning the coupling ratio and, consequently, the Q-factor of the microresonators designed to compensate the dispersion of optical fiber communication lines [80]. Such application utilized AMZI's amplitude response properties. We propose to use AMZI's phase response for equalizing the resonance spacing, which would effectively mitigate the dispersion of the group refractive index inside the microresonator.

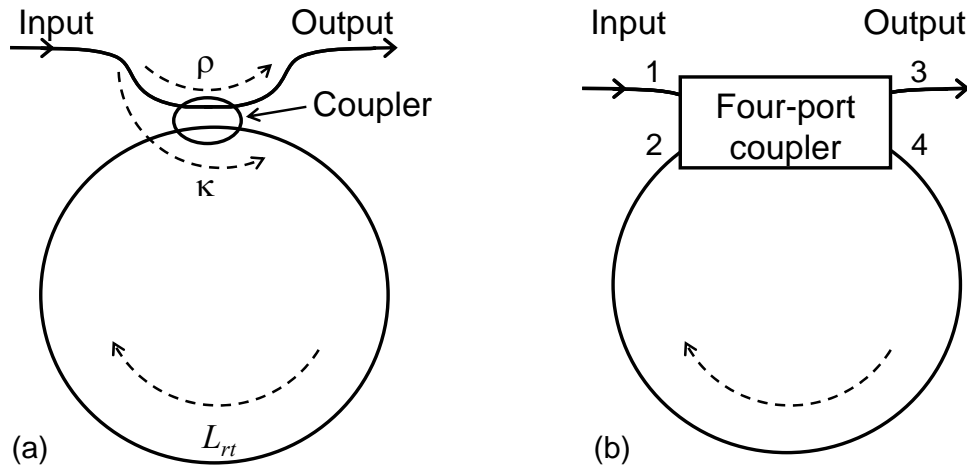


Figure 4-1. (a) Microresonator with simple input / output coupler, described by Eq. (4.1). (b) Similar microresonator, in which simple coupler has been replaced by a more general four-port coupler, which may have frequency-dependent amplitudes and phases of the coupling and reflection coefficients.

4.1. Mode spacing in a micro resonator

Electric field inside a microresonator E_{inside} is related to the input field E_{input} as

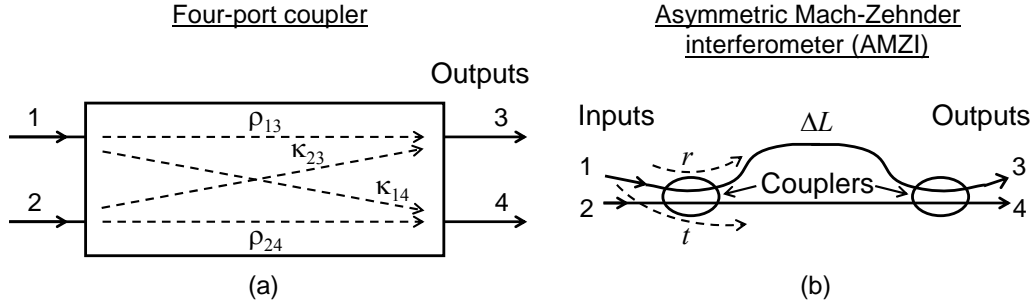


Figure 4-2. (a) Definition of coupling and reflection coefficients of a general four-port coupler. (b) Implementation of a four-port coupler by an asymmetric Mach-Zehnder interferometer (AMZI) with ΔL path difference between its two arms.

$$E_{\text{inside}} = \frac{E_{\text{input}} \kappa}{1 - \rho e^{i\varphi(\omega)} e^{-\varepsilon/2}}, \quad (4.1)$$

where κ and ρ are, respectively, the coupling and reflection coefficients of the input / output coupler ($|\kappa|^2 + |\rho|^2 = 1$), as shown in Fig. 4-1(a), ε is the round-trip loss of the cavity (intensity of the wave goes down by $e^{-\varepsilon}$ after each round trip), and

$$\varphi(\omega) = \beta(\omega)L_{rt} \quad (4.2)$$

is the cavity round-trip phase accumulation [here $\beta(\omega)$ is the waveguide propagation factor, ω is the frequency of light wave, and L_{rt} is the round-trip cavity length]. Resonance frequencies ω_m are obtained from the condition

$$\varphi(\omega_m) = \beta(\omega_m)L_{rt} = 2\pi m. \quad (4.3)$$

For small detunings ($\omega - \omega_m$) from resonance frequency ω_m ,

$$\beta(\omega) \approx \beta(\omega_m) + \beta'(\omega_m) \times (\omega - \omega_m), \quad (4.4)$$

where

$$\beta' = d\beta/d\omega = 1/v_g = n_g/c, \quad (4.5)$$

v_g is the group velocity of the mode, n_g is the mode's group index

$$n_g(\omega) = n_{\text{eff}}(\omega) + \omega \frac{dn_{\text{eff}}(\omega)}{d\omega}, \quad (4.6)$$

and $n_{\text{eff}} = \beta(\omega) / (\omega/c)$ is the effective index of the mode. Then, we have

$$\beta(\omega_{m+1})L_{rt} - \beta(\omega_m)L_{rt} = \beta'(\omega_m) \times (\omega_{m+1} - \omega_m)L_{rt} = 2\pi, \quad (4.7)$$

or

$$\Delta\omega_{\text{FSR}} = \omega_{m+1} - \omega_m = \frac{2\pi c}{n_g(\omega_m)L_{rt}}, \quad (4.8)$$

where $\Delta\omega_{\text{FSR}}$ is the free-spectral range (FSR, or frequency spacing between the adjacent modes) of the microresonator. Thus, the frequency spacing depends on the group index of the waveguide and hence may change owing to non-zero value of the group velocity dispersion

$$\begin{aligned} \beta''(\omega) &= \frac{d\beta'(\omega)}{d\omega} = \frac{1}{c} \frac{dn_g(\omega)}{d\omega} \\ &= -\frac{2\pi c}{\omega^2} D = -\frac{\lambda^2}{2\pi c} D, \end{aligned} \quad (4.9)$$

where D , usually expressed in ps/nm/km, is the most common notation of the dispersion in optical communications field, and λ is the wavelength of light.

In order to equalize the frequency spacings among the modes (i.e., effectively make the group index independent of frequency), we propose to utilize an intracavity element whose dispersion would cancel or nearly cancel D in the wavelength range of our practical interest. Such an additional element would result in an additional factor $e^{i\psi(\omega)}$ next to $e^{i\phi(\omega)}$ in the denominator of Eq. (4.1), representing the phase response of the element. In order to cancel the dispersion D , the second derivative of $\psi(\omega)$ should cancel the second derivative of $\phi(\omega)$, i.e.,

$$\frac{d^2\psi(\omega)}{d\omega^2} = -\frac{d^2\phi(\omega)}{d\omega^2} = -\beta''(\omega)L_{rt} = \frac{2\pi c}{\omega^2}DL_{rt} = \frac{\lambda^2}{2\pi c}DL_{rt}. \quad (4.10)$$

It is possible to achieve such a cancellation effect even without inserting any extra dispersive element into the cavity: one just needs to employ a dispersive input/output coupler, i.e., the coupler with $\rho(\omega)=|\rho(\omega)|e^{i\psi(\omega)}$ [the microresonator with a general four-port coupler is shown in Fig. 4-1(b), and the definitions of its reflection and coupling coefficients are shown in Fig. 4-2(a)]. Such a coupler can be made out of an asymmetric Mach-Zehnder interferometer (AMZI), shown in Fig. 4-2(b).

Indeed, for an AMZI, where both input and output couplers have the coupling and reflection coefficients $t = \sqrt{T}$ and $r = \sqrt{1-T}$, respectively, and $\delta = n_{\text{eff}}\Delta L$ (where ΔL is the length difference between the long and short arms), the input and output are related by the following frequency-dependent coupling and

reflection coefficients [here, we omit the common propagation phase of all these coefficients, because it has already been included into the total roundtrip phase of Eqs. (4-1)–(4-2)]:

$$\begin{aligned}
\rho_{24}(\omega) &= t^2 e^{i\omega\delta/c} + r^2 = T e^{i\omega\delta/c} + 1 - T, \\
\kappa_{14}(\omega) &= \kappa_{23}(\omega) = rt(1 - e^{i\omega\delta/c}) = \sqrt{T(1-T)}(1 - e^{i\omega\delta/c}), \\
\rho_{13}(\omega) &= r^2 e^{i\omega\delta/c} + t^2 = (1-T)e^{i\omega\delta/c} + T,
\end{aligned} \tag{4.11}$$

and $|\kappa_{14}\kappa_{23} - \rho_{13}\rho_{24}| = 1$. Hence, the reflection coefficient $\rho(\omega)$ in Eq. (4-1) should be replaced by $\rho_{24}(\omega) = |\rho_{24}(\omega)|e^{i\psi(\omega)}$ from Eq. (4-11), whose phase response $\psi(\omega)$ is given by

$$\psi(\omega) = \tan^{-1} \left[\frac{T \sin(\omega\delta/c)}{T \cos(\omega\delta/c) + 1 - T} \right], \tag{4.12}$$

and its second derivative is given by

$$\begin{aligned}
\frac{d^2\psi(\omega)}{d\omega^2} &= - \left(\frac{n_g \Delta L}{c} \right)^2 T(1-T)(1-2T) \frac{\sin \gamma}{\left[1 - 4T(1-T)\sin^2(\gamma/2) \right]^2} \\
&\quad - \frac{\lambda^2 D}{2\pi} \frac{\Delta L}{c} T \frac{1 - 2(1-T)\sin^2(\gamma/2)}{1 - 4T(1-T)\sin^2(\gamma/2)},
\end{aligned} \tag{4.13}$$

where $\gamma = \omega\delta/c$, and the second line of Eq. (4-13) is a relatively small contribution of the effective index dispersion to the total dispersion of the AMZI. Combining Eqs. (10) and (13) yields the values of dispersion D that can be compensated by the AMZI at different frequency regions of the spectrum of its reflection

coefficient $\rho_{24}(\omega)$. Since the AMZI's dispersion of Eq. (4-13) is frequency-dependent, it will not be able to perfectly compensate dispersion for all frequencies. However, because the round-trip length of the microresonator L_{rt} is much greater than the AMZI path length difference ΔL :

$$N = L_{rt} / \Delta L \gg 1, \quad (4.14)$$

the frequency range for which the dispersion is well compensated can be rather wide (many times the FSR $\Delta\omega_{\text{FSR}}$). We can express the result in terms of N , γ and $\Delta\omega_{\text{FSR}}$ as follows:

$$\begin{aligned} D_{\text{compensated}} &= \frac{d^2\psi(\omega)}{d\omega^2} \frac{2\pi c}{\lambda^2 L_{rt}} \\ &= -\frac{T(1-T)(1-2T)\sin\gamma}{[1-4T(1-T)\sin^2(\gamma/2)]^2} \left(\frac{2\pi}{\lambda N}\right)^2 \frac{n_g}{\Delta\omega_{\text{FSR}}} \times \left[1 + \frac{T}{N} \frac{1-2(1-T)\sin^2(\gamma/2)}{1-4T(1-T)\sin^2(\gamma/2)}\right]^{-1}. \end{aligned} \quad (4.15)$$

We can further rewrite the results by expressing both φ and γ in terms of the normalized detuning from the m^{th} resonance of the microresonator

$$\theta = \frac{n_g \Delta L}{c} (\omega - \omega_m). \quad (4.16)$$

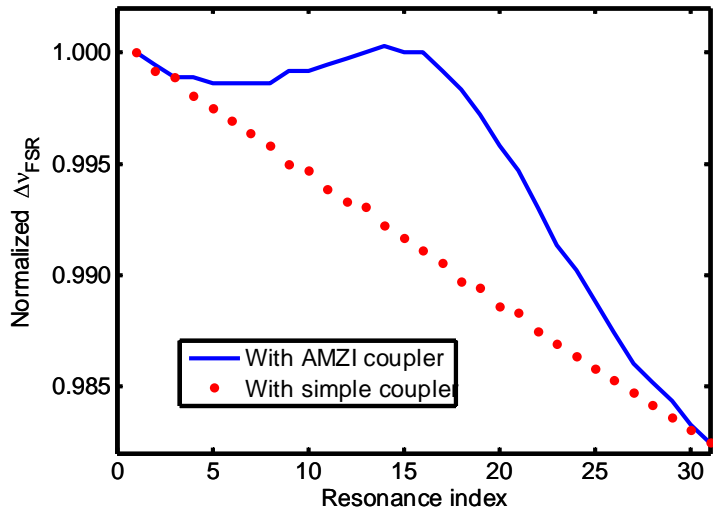
Expanding both φ and γ in Taylor series up to the second order (to account for dispersion), we have

$$\begin{aligned}
\varphi(\omega) &= \varphi(\omega_m) + \beta'(\omega_m)(\omega - \omega_m)L_{rt} + \beta''(\omega_m)\frac{(\omega - \omega_m)^2}{2}L_{rt} \\
&= 2\pi m + \frac{n_g L_{rt}}{c}(\omega - \omega_m) - \frac{\lambda^2 D L_{rt}}{4\pi c}(\omega - \omega_m)^2 \\
&= 2\pi m + N\theta - \frac{\lambda^2 D \Delta\omega_{FSR}}{8\pi^2 n_g} N^2 \theta^2, \tag{4.17}
\end{aligned}$$

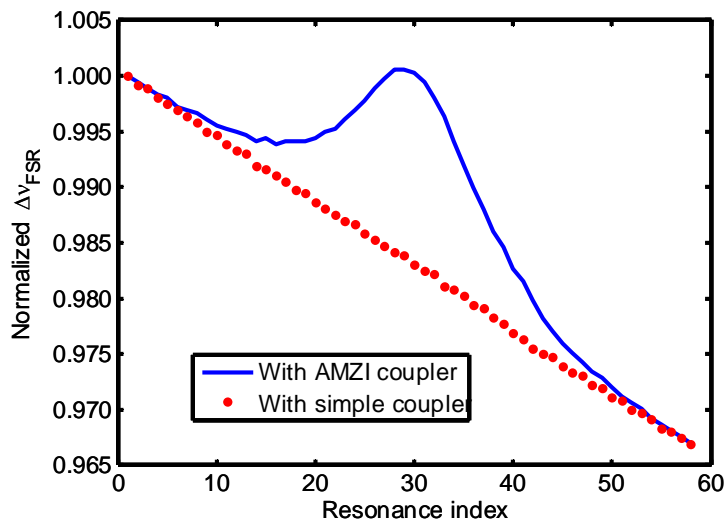
$$\begin{aligned}
\gamma(\omega) &= \varphi(\omega) / N \\
&= \gamma(\omega_m) + \theta - \frac{\lambda^2 D \Delta\omega_{FSR}}{8\pi^2 n_g} N \theta^2.
\end{aligned}$$

Owing to the periodic phase response of both the microresonator and the AMZI, it is sufficient to consider only the range of $\theta = 0 \dots 2\pi$, which covers approximately one free spectral range (period) of the AMZI spectrum and N free spectral ranges (periods) of the microresonator.

The modeling results are shown in Figure 4-3. The blue line represents the normalized value of the change in the free spectral range for an AMZI coupler, and the dotted red line shows the same for a simple coupler. We can easily see that the compensation of dispersion inside the microresonator by means of an AMZI's phase response results in compression of the variations of $\Delta\nu_{FSR}$ from $\pm 0.50\%$ to $\pm 0.07\%$ for the first 17 resonances in Figure 4-3(a) and from $\pm 1.0\%$ to $\pm 0.3\%$ for the first 34 resonances in Figure 4-3(b).



(a)



(b)

Figure 4-3. Modeling results of the change in the free spectral range for different resonances (blue curve), with red dots representing a microresonator with a simple coupler. Parameters: (a) $N=31$ and $T=0.13$. (b) $N=61$ and $T=0.3$.

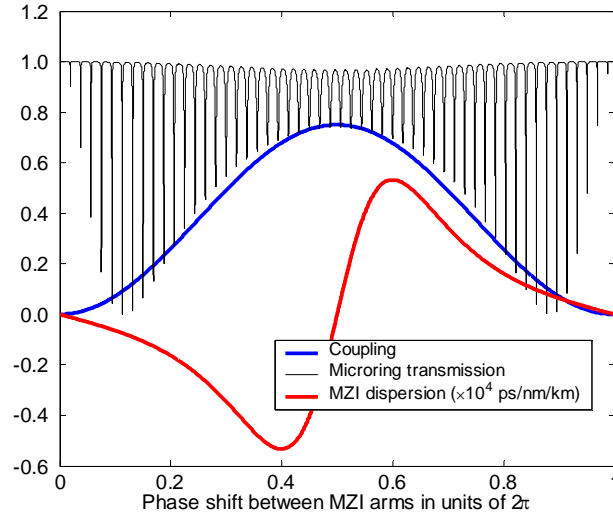
In Figure 4-4(a) we plot the normalized dispersion of the AMZI coupler (red curve), given by Eq. (4-14) normalized by a factor $2D$, and the transmittance

$$T_{\text{total}} = \left| \frac{E_{\text{output}}}{E_{\text{input}}} \right|^2 = \left| \frac{\rho_{13} - e^{i(\gamma+\phi)} e^{-\varepsilon/2}}{1 - \rho_{24} e^{i\phi} e^{-\varepsilon/2}} \right|^2 \quad (4.18)$$

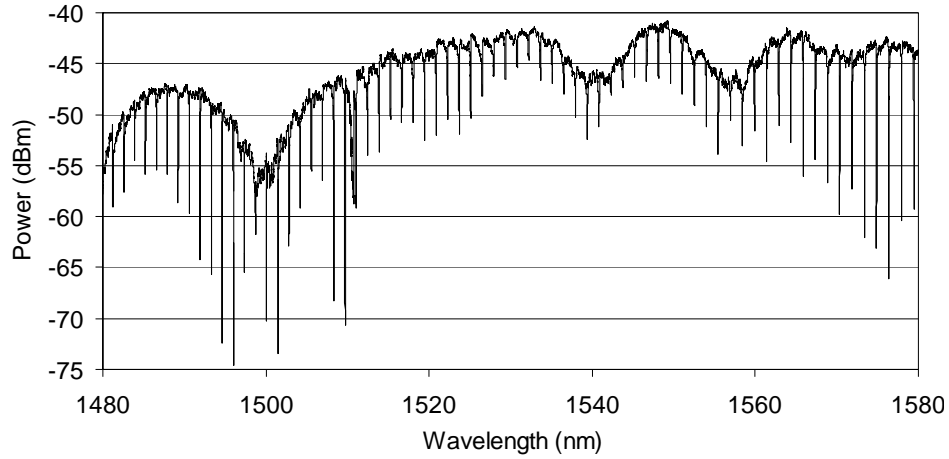
of the microresonator with AMZI coupler (solid black curve) as functions of θ , with $\gamma(\omega_m)$ chosen to be a multiple of 2π . The envelope of the resonance minima roughly follows the spectral shape of the AMZI power coupling coefficient $|\kappa_{14}|^2 = 1 - |\rho_{24}|^2$ throughout middle three quarters of the spectrum. At the center of the spectrum the cavity is over-coupled, and the resonances are not deep. As one moves away from the middle of the spectrum, the coupling approaches the intra-cavity loss (critical coupling), and the resonances become deeper. On the far left and right sides the resonances become shallow again, because the coupling becomes very small (under-coupled cavity).

4.2. Experimental Results

Experimentally measured transmission of the microresonator with AMZI coupler is shown in Figure 4-4(b). As noted in the theory, the microresonator goes from over-coupled region around 1480 nm to critically-coupled region around 1500 nm. It further goes to under-coupled region around 1540 nm and goes back to critically-coupled region around 1570 nm.

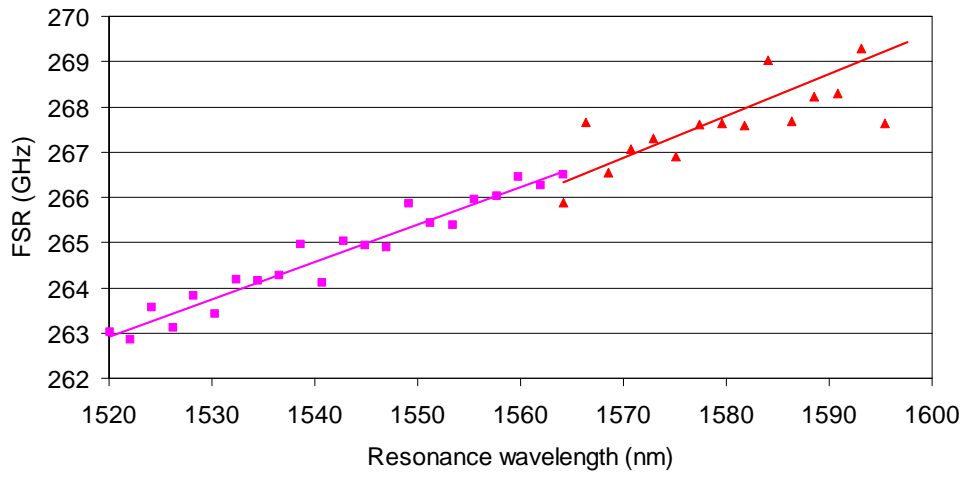


(a)

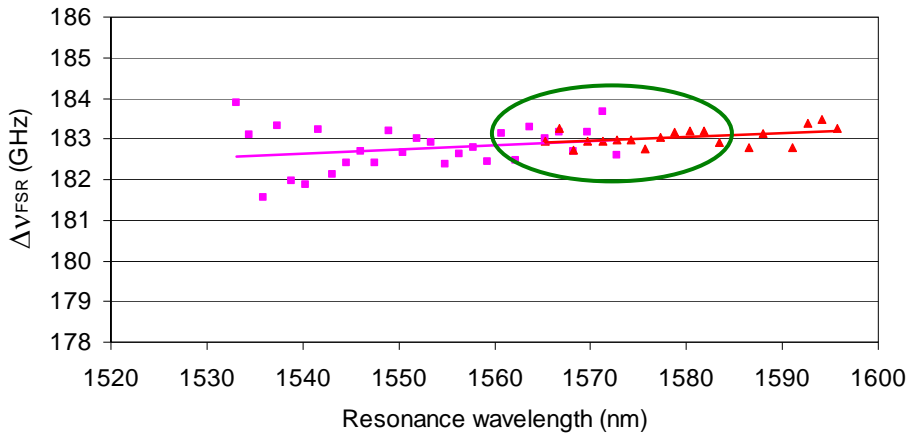


(b)

Figure 4-4. (a) Transmittance of the microresonator (solid black), power coupling coefficient $|\kappa_{14}|^2 = 1 - |\rho_{24}|^2$ of the AMZI coupler (blue), and normalized dispersion of the AMZI coupler $D_{\text{compensated}} / (2D)$ (dot-dashed red), obtained with $D = -2000$ ps/nm/km, $\Delta\nu_{\text{FSR}} = 200$ GHz, $\lambda = 1550$ nm, $n_g \approx 1.6$, $\varepsilon = 0.1$, $N = 34$, and $T = 0.13$. (b) Experimentally measured spectrum of the transmittance of a Si_3N_4 microresonator with AMZI coupler, with $\Delta\nu_{\text{FSR}} \approx 180$ GHz and $N \approx 50$. Normalized frequency detuning θ is defined by Eq. (4.16).



(a)



(b)

Figure 4-5. (a) Frequency spacings Δv_{FSR} for a Si_3N_4 microresonator with a simple coupler, indicating waveguide dispersion $D \approx -2000$ ps/nm/km. (b) Frequency spacings Δv_{FSR} for a Si_3N_4 microresonator with AMZI coupler with $N \approx 50$.

Figure 4-5 shows the experimentally measured values of the resonance spacing Δv_{FSR} in a silicon-nitride microresonator (a) without and (b) with AMZI coupler.

One can see the reduction of the dispersion inside the microresonator from -2000 ps/nm/km to -350 ps/nm/km over whole C+L band or even to ± 100 ps/nm/km within 1560 ... 1590 nm range (green circle).

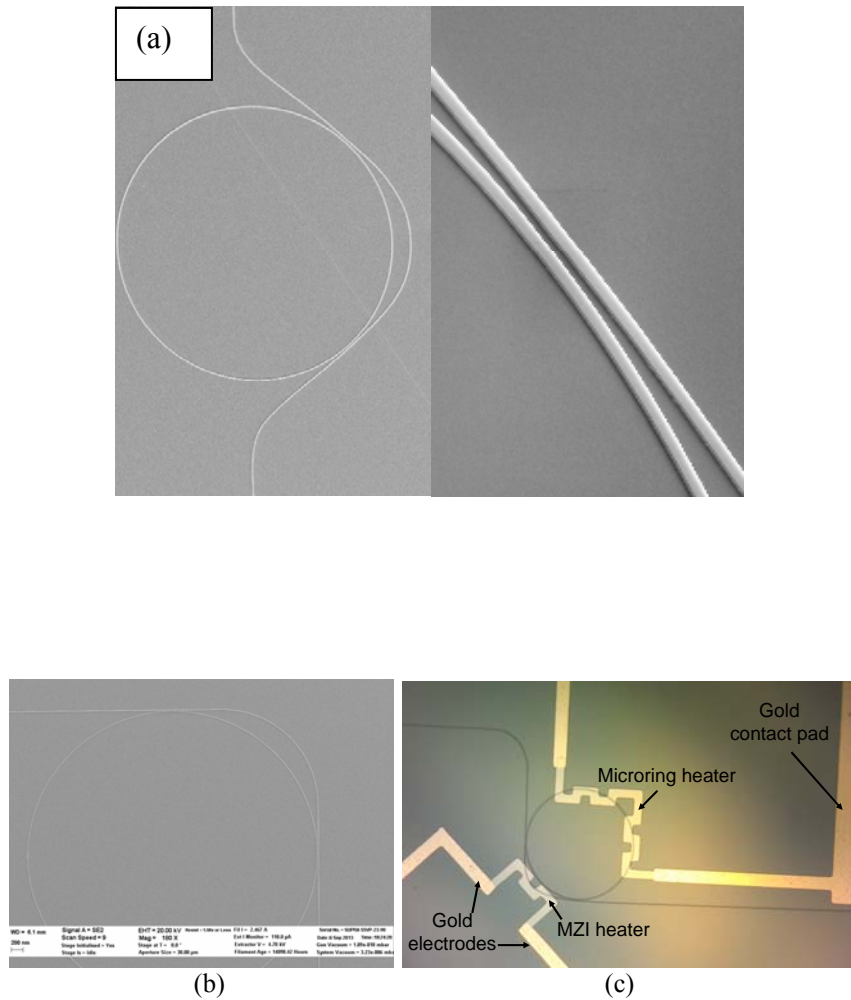


Figure 4-6. (a),(b) Scanning electron microscope (SEM) images of fabricated Si_3N_4 microresonators with AMZI couplers and different length differences between the long and short arms ΔL . (c) Optical microscope image of the fabricated Si_3N_4 microresonator with an AMZI coupler after deposition of the heating electrodes used for separate tuning of the AMZI and the microresonator.

Further flexibility can be obtained by adding micro heaters to the coupler and the microring resonator as shown in Figure 4-6(c). By reasonable heating of the microresonator one can shift all resonances by approximately one free spectral range $\Delta\nu_{\text{FSR}}$. A separate heater for the AMZI coupler allows shifting the position of the minimum of its coupling $|\kappa_{14}|^2 = 1 - |\rho_{24}|^2$ (i.e., transmittance from port 1 to port 4 of the coupler) in order to align the spectral region where it compensates the dispersion (approximately the region from the minimum to the maximum of its coupling coefficient) with the spectral region of interest.

4.3. Summary

In this chapter the theoretical background of a microring resonator in an asymmetric Mach-Zehnder configuration has been introduced, and the modeling results for a dispersive coupler have been explained. We have experimentally demonstrated the reduction of the dispersion from -2000 ps/nm-km (microring with a simple coupler) to within ± 100 ps/nm-km over a 30-nm-wide wavelength span (microring with an asymmetric Mach-Zehnder coupler), which shows that the dispersion in microrings can be compensated with our dispersive coupler design.

CHAPTER 5

CONCLUSION

“On-chip” optical sources generating frequency combs by nonlinear interaction of the electromagnetic waves via higher-order susceptibilities of materials are currently under active investigation. We believe that the $\chi^{(3)}$ material properties of silicon nitride offer excellent scope for operating in high optical intensity regimes to generate new frequencies without any drawbacks of two-photon absorptions and other nonlinear losses. Among the different device geometries considered for this process, microring resonators have attracted a lot of attention because of their small foot print and the feasibility of achieving high quality factors using the standard CMOS process. With effective areas of less than $0.5 \mu\text{m}^2$ and cavity-enhanced field build-up, the microring resonators are perfect choice for generating on-chip frequency combs and entangled photon pairs aimed at quantum communication applications. This dissertation discusses the fabrication methodology of silicon nitride based microring resonators, and our measurements of their resonance characteristics, delay line, and dispersion properties are presented. The highest quality factor we measured in our fabricated microring resonators was up to 8×10^4 with free spectral range of 180 GHz at 1550 nm, with the ring resonator waveguide loss of 0.4 dB/mm. Microring resonators can also be used for dispersion compensation applications in telecommunication.

The dispersion in these microrings is known to be a limitation, because it results in the unequal free spectral range across a broad spectrum of wavelengths. Conventional method to avoid this is depositing thick silicon nitride films, so that most of the mode is confined within the waveguide core, reducing the waveguide dispersion. But this method involves a complicated fabrication process owing to the mechanical stress in thick silicon nitride films. Instead, we have proposed and experimentally demonstrated a new scheme involving a microring with a dispersive coupler in an asymmetric Mach-Zehnder interferometer configuration and showed compensation of the microring dispersion in such a scheme. The results show that a microring resonator with a simple coupler had the dispersion value of -2000 ps/nm-km. When this microring is incorporated into the scheme with an asymmetric Mach-Zehnder interferometric coupler, the dispersion is reduced to a value within ± 100 ps/nm-km, which indicates a significant reduction in the dispersion.

These results show a great promise of microrings with the asymmetric Mach-Zehnder interferometer couplers for potential applications in generating frequency combs and entangled photon pairs. By further incorporating thermal tuning of microrings, the operating wavelength regions can also be adjusted.

APPENDIX A
PULSE PICKER DRIVER FOR POCKELS CELL

We are interested in the applications of high-frequency pulse generators in driving laser diodes and modulators for studying fast phenomenon in quantum dots and fluorescent decays. We have developed a high-voltage pulse driver to drive an electro-optic modulator (a Pockels cell), which needs duration of the shutter opening less than 5 ns and a driving voltage of 150 V to select a lower-repetition-rate sequence of pulses from an optical parametric oscillator synchronously pumped by a mode-locked laser with repetition frequency of 76 MHz. The signal from the monitor photodiode from the laser serves as the input to the pulse picker instrumentation module to drive the Pockels cell. The experimental schematic is shown in the Figure A-1.

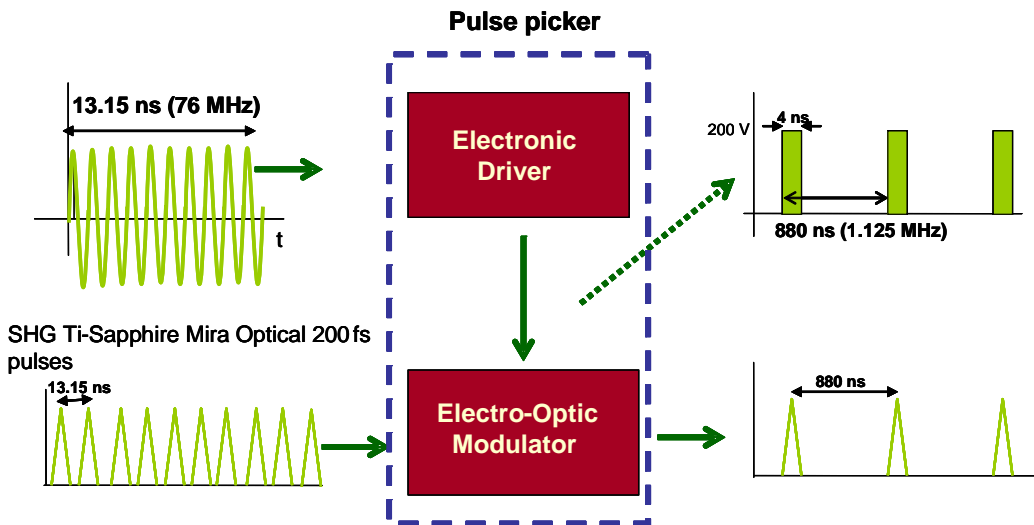


Figure A-1. Schematic of operation of pulse picker.

Since our existing Pockels cell requires a V_{π} voltage of greater than 150 V, the unit is designed to deliver very sharp pulses (less than 4 ns rise time) at two different pulse repetition rates, depending upon the selection knob. The Pockels cell needs two outputs from the box: high-voltage pulse and bias voltage. The box delivers these two and also a third output, which is a simple square wave at two different frequencies. This output is not required to drive the Pockels cell.

A.1. Description of the pulse generator:

Pulse picker, control unit box has **one** input and **three** outputs.

The unit can take input signal (input) up to 156 MHz in frequency with peak-to-peak voltages between 40 mV and 1 V and give an output signal with pulse raise time less than 4 ns and 200 V amplitude with two varieties of pulse repetition frequencies, depending upon the selection with the knob.

The three outputs are...

1. High voltage pulse output.
2. Modulator bias output.
3. Square wave output.

The square wave output gives two different frequencies of square waves depending upon a selection knob position, when an input signal is present. The PRF (pulse repetition frequency) of the “high-voltage output pulse” is half of the PRF of this “square wave output”.

Four separate PCBs are built and assembled inside a box. These PCBs are designed for the following purposes:

1. Frequency-divider PCB.
2. High-voltage amplifier PCB.
3. Voltage-regulator PCB
4. Bias-control PCB

Voltage-regulator PCB has two output voltages. One is 80 V DC and other is an adjustable output voltage with a potentiometer with max output of 11.4 V. The output 1 powers the RF amplifier. The frequency dividers are powered by fixed 5 V by a separate power supply.

The second PCB has two outputs. One goes in to the amplifier PCB and other goes into the output panel.

A.2. Frequency-divider PCB

The frequency-divider PCB contains an RF amplifier (SGA 6589) and two clock divider ICs (IC 542). The reason an RF amplifier is used ahead of the clock divider ICs is because the clock divider IC requires the input signal to be minimum of 500 mV for it to function accurately. Since the signal fed to the front panel of the control unit could be a weak signal (from a photo detector output in our experiment), the inside RF amplifier would amplify such a weak signal and is compatible for the frequency divider IC to function properly. The gain of the RF amplifier is fixed, and the value is 28.4 at 100 MHz. The expected minimum

input signal amplitude for this amplifier in the experiment is 50 mv at 80 MHz.

A.3. RF amplifier

The RF amplifier IC used is SGA 6589. The schematic is as follows. The input signal is capacitively coupled to the IC by a 1200 pF capacitor. The series resistor used is 100 Ω , which is chosen according to the frequency of operation. A set of appropriate values for different frequencies is given in the datasheet. This is powered by a 12 V power supply inside. The output of the amplifier is coupled to the frequency divider circuit by a capacitor of 1200 pF.

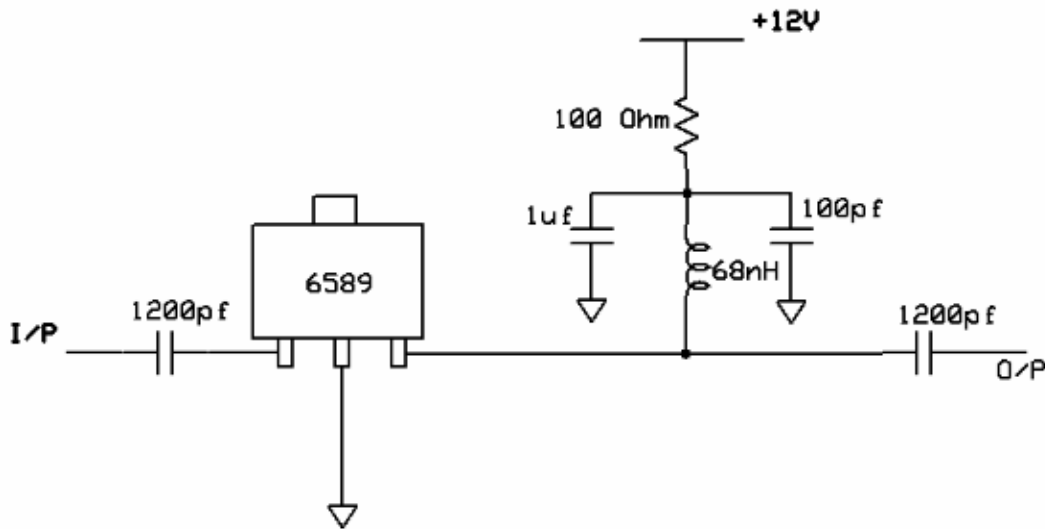


Figure A-2. Schematic for the RF amplifier circuit to amplify the output from photodiode of an OPO (optical parametric oscillator).

A.4. Frequency divider

This is basically a clock divider circuit. The final output of the box gives a high-

voltage pulses of two different frequencies, one is $f / 72$ and other is $f / 96$ (determined by the selecting knob at the front panel) where f is the input frequency in to the box. So this sort of frequency division is achieved by two ICs IC 542. IC 542 is an 8 pin IC with two clock division controls. Such two ICs are used to achieve a very low clock rate output. These ICs are operated in single supply by 5 V supply P2. Both ICs are given a 0.01 μ F decoupling capacitors. The 7th pin of the IC 542 is a high impedance pin, which has to be floating. If it is grounded the IC will be powered down. The two ICs are coupled by a 1200 pF capacitor. Each of the IC 542 has two outputs one of them that gives half of the other one's frequency. For the first IC, only one of the outputs is used and is coupled to the second IC 542. In the second clock divider IC both outputs are used. One of the outputs is given to the front panel by which the unit gives a pure square wave output at frequency $f / 36$ or $f / 48$, depending upon the knob setting. The corresponding second output, which gives either $f / 72$ or $f / 96$ (determined by the knob), is fed next to the high-voltage amplifier PCB by a coaxial cable.

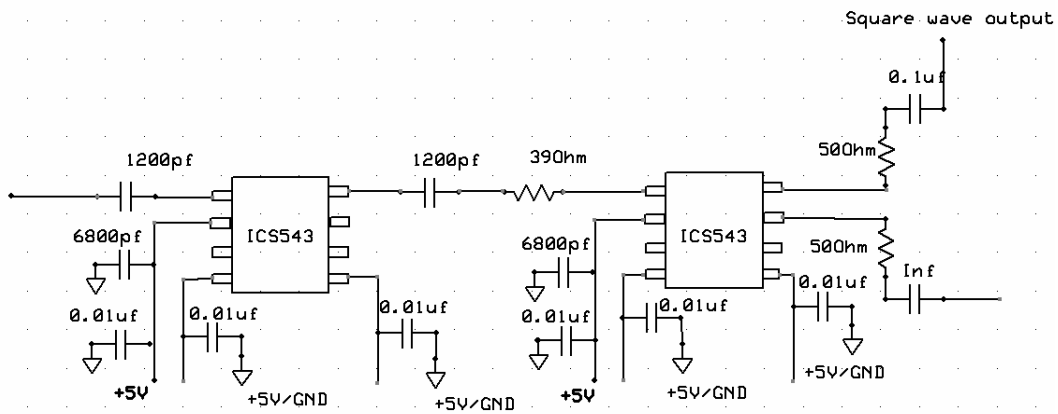


Figure A-3. Circuit schematics of frequency dividers.

A.5. High-voltage amplifier PCB

This PCB is the one that amplifies a 2 V, $f/72$ or $f/96$ square wave signal to a 200 V unipolar pulse with a rise time of 4 ns. This is achieved by a series of transistors and MOSFETS. The main part of this PCB is two P-channels and one N-channel MOSFETS. Before these MOSFETS there is a two-stage complementary NPN and PNP pair. The transistors used here are P2N2222 (NPN) and 2N2905A (PNP). These two stages amplify the incoming signal to a 12 V 40 ns unipolar pulse. The transistor biasing is chosen in such a way that the operating point is in saturation regime. Each transistor is in saturation regime and switch between 0 V and 12 V (supply voltage V_{cc}). For these two stages, the transistor biasing resistor with a capacitor forms an RC combination and by choosing very small values of the capacitors and appropriate resistors sharp pulse

of 40 ns duration and 12 V is achieved at the end of the second stage complementary pair. The schematic is shown in Figure A-4.

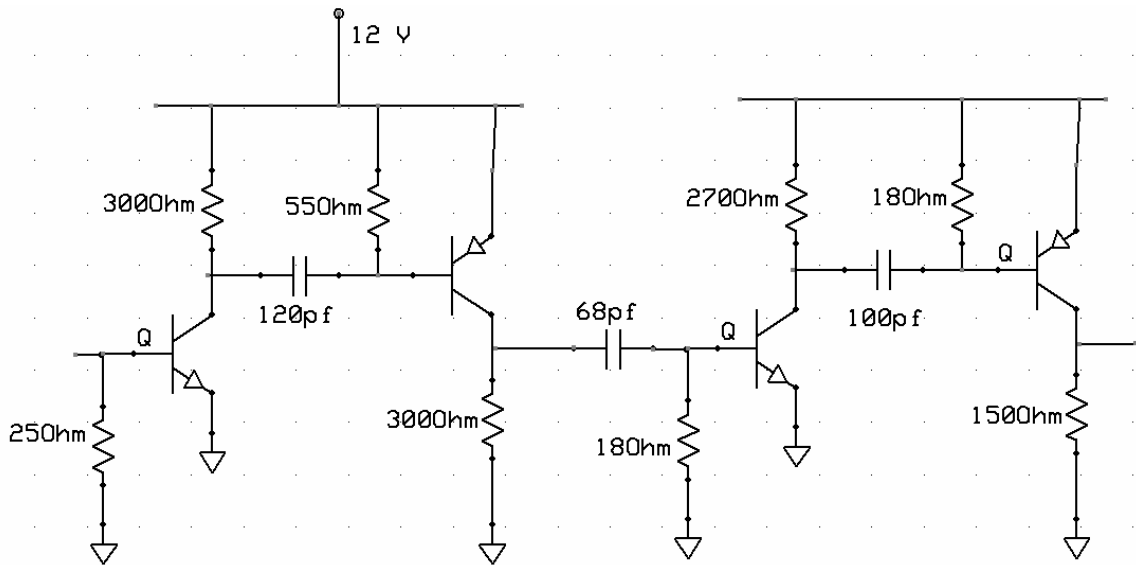


Figure A-4. Schematic showing transistors in complimentary scheme.

This signal is coupled to the gate of the IRF 5801 high voltage N-channel MOSFET with a 220 pF capacitor . The bias resistor used here is 560 Ω . The V_{DSS} of this MOSFET is 200 V and the gate capacitance is 88 pF. Thus, this is a high-speed transistor that can handle DC voltage up to 200 V. There are two IRF 5801 MOSFETs in the circuit. In between these two N-channel MOSFETs there is IRF 6217, a P-channel MOSFET. So, as the pulse travels through these transistors and MOSFETs, its polarity keeps flipping.

In the entire circuit, capacitor and resistor values are optimized keeping in mind three objectives.

- (i) To obtain high voltage pulse (> 150 V).
- (ii) To obtain very sharp pulse width

(4 ns). (iii) Low heating effects of the components. To obtain these objectives, several values of capacitors and resistors, as well as voltage values, are tried, and the pulse is checked at each and every node.

The first IRF 5801 and IRF6217 are powered by an 80 V supply instead of 200 V. Only the last MOSFET in the circuit, which is IRF 5801, is powered by 200 V. This is done because the first two MOSFETS get very hot because of the large pulse widths driving them. The pulse width of the signal gets smaller and smaller as it reaches the final stages. Therefore, to avoid the heating, the first two MOSFETS are powered by 80 V supply. The reason for choosing 80 V is that optimizing for the maximum amplitude for the final pulse at the same time minimizes the heating of the MOSFETS. The top body of these MOSFET ICs is glued with silver paint mixed with commercially available SuperGlue epoxy to a small metallic heat sink plate. A 3500 RPM fan is mounted on the top of this PCB for cooling.

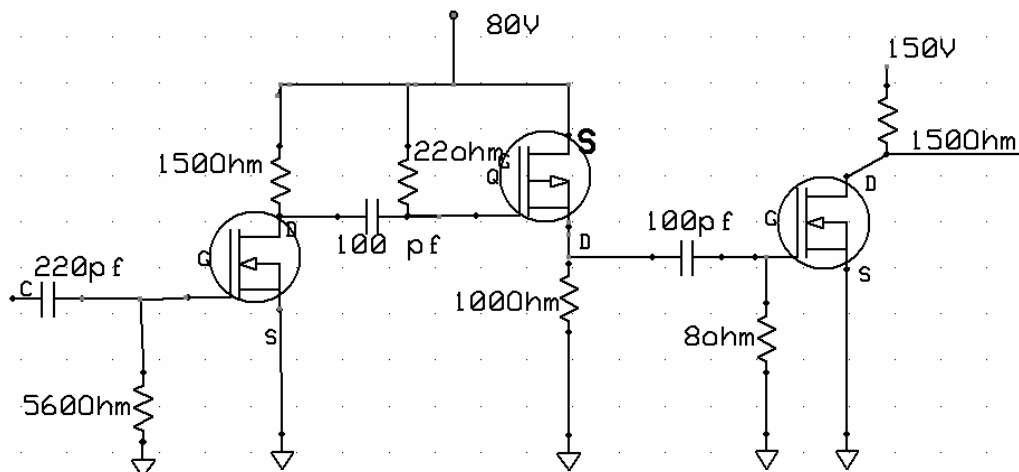


Figure A-5. Schematc showing MOSFETS generating high voltage.

A.6. Voltage-regulator PCB

This PCB has two voltage regulators with two different power supplies. (a) One is a 12 V supply, and the voltage regulator is LM317. This regulator has a potentiometer, by which the output voltage can be adjusted. This is implemented to give flexibility in giving desired voltage to the initial RF amplifier. (b) The second voltage regulator is LR8, a high-voltage regulator. This is used to supply an 80 V source to power the two MOSFETs. The LR8 voltage regulator's current delivery ability is only 20 mA maximum. Thus, along with this voltage regulator, a power transistor (NPN) TIP50 is also used as a pass transistor to obtain a maximum current of 120 mA. The schematic for these two regulators is given below.

A.7. Bias-control PCB

This PCB gives a regulated voltage output, adjustable between values 6 V and 188 V. A 2 W, 10 turn 100 k Ω potentiometer attached to the front panel is used to set the desired bias voltage. The regulator used in this PCB is LR8. The front panel has a BNC connector through which this DC bias voltage can be obtained.

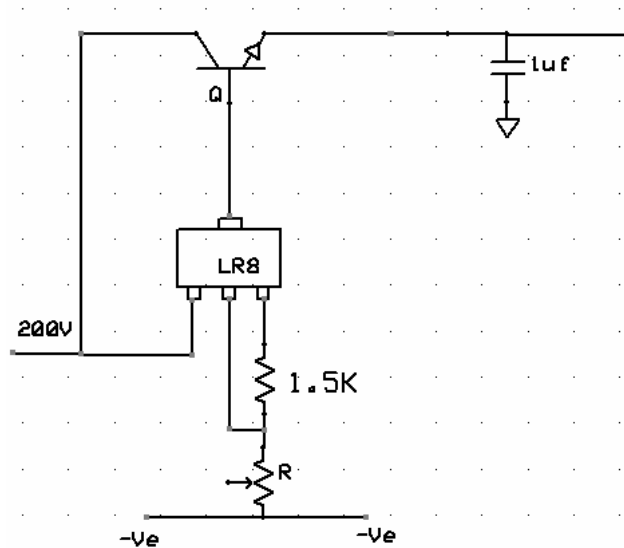


Figure A-6. Schematic showing the bias-control PCB.

A.8. Power supplies and chassis of the box

The pulse picker control unit box has two power supplies inside. Both of these power supplies are powered by external 120 V AC voltage from the wall outlet. The chassis (body) of the box is grounded. The two power supplies inside are as follows.

1. 200 V, 0.12 A
2. 12 V , 1 A and 5 V , 2.5 A.

The 200 V supply has a built-in adjustable potentiometer, by which the DC

voltage output can be adjusted between 150 V and 200 V. This power supply powers three MOSFETs and the DC bias PCB. The 12 V supply powers the initial RF amplifier, clock divider, and two stage NPN-PNP complementary pair, which is before the MOSFETs.

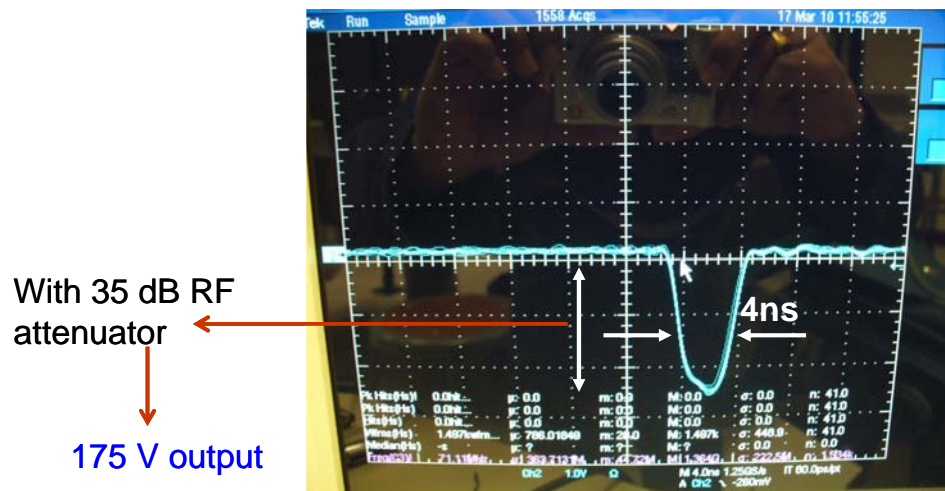


Figure A-7. Photograph showing the pulse on the oscilloscope.

A.9. Conclusion

The pulse picker control unit box is tested at a maximum input frequency of 80 MHz. The obtained maximum final output repetition rate is 1.11 MHz ($f/72$), and the device can generate pulses of 4 ns duration with 170 V amplitude. This utilizes 120 mA maximum of the power supply. A higher repetition rates up to 2.5 MHz can also be obtained with the same design, with a power supply having

specifications to deliver 300 mA.

General specifications of the unit:

	<u>VALUE</u>
1. Max input signal voltage:	1 V _{pp}
2. Input frequency range	1 MHz –156 MHz
3. Output pulse rise time	4 ns
4. Output pulse voltage	170 V
5. High-voltage output pulse PRF	$f/72$ and $f/96$

Specifications of Power supplies inside:

200 V power supply :

Max output voltage: 170 V (adjustable from 150 V to 170 V with inside potentiometer).

Maximum output current: 0.12 A

12 V / 5 V supply :

Two voltage outputs.

(i) 12 V, 1 A

(ii) 5 V, 2.5 A

REFERENCES

- [1] Tien, P. K., R. Ulrich, and R. J. Martin. "Modes of propagating light waves in thin deposited semiconductor films." *Applied Physics Letters* 14.9 (1969): 291-294.
- [2] Shubert, R., and H. Harris. "Optical surface waves on thin films and their application to integrated data processors." *Microwave Theory and Techniques, IEEE Transactions on* 16.12 (1968): 1048-1054.
- [3] Hall, David, Amnon Yariv, and Elsa Garmire. "Observation of propagation cutoff and its control in thin optical waveguides." *Applied Physics Letters* 17.3 (1970): 127-129.
- [4] Moore, Gordon E. "Cramming more components onto integrated circuits," Reprinted from *Electronics*, volume 38, number 8, April 19, 1965, pp. 114 ff." *IEEE Solid-State Circuits Newsletter* 3.20 (2006): 33-35..
- [5] Alduino, Andrew, and Mario Paniccia. "Interconnects: Wiring electronics with light." *Nature Photonics* 1.3 (2007): 153-155.
- [6] R. Soref, "The past, present, and future of silicon photonics," *IEEE J. Sel. Top. Quantum Electron.* 12, 1678–1687 (2006).

- [7] Assefa, Solomon, et al. "A 90 nm CMOS integrated nano-photonics technology for 25 Gbps WDM optical communications applications." Electron Devices Meeting (IEDM), 2012 IEEE International. Vol. 33. IEEE, 2012.
- [8] Knoll, Dieter, et al. "Monolithically integrated 25Gbit/sec receiver for 1.55 μm in photonic BiCMOS technology." Optical Fiber Communication Conference. Optical Society of America, 2014.
- [9] Vlasov, Yurii A. "Silicon CMOS-integrated nano-photonics for computer and data communications beyond 100G." Communications Magazine, IEEE 50.2 (2012): s67-s72.
- [10] Lee, Byeong, et al. "Monolithic silicon integration of scaled photonic switch fabrics, CMOS logic, and device driver circuits." Lightwave Technology, Journal of 32.4 (2014): 743-751.
- [11] Liao, Liu, et al. "40 Gbit/s silicon optical modulator for highspeed applications." Electronics letters 43.22 (2007)
- [12] Gardes, F. Y., et al. "40 Gb/s silicon photonics modulator for TE and TM polarisations." Optics express 19.12 (2011): 11804-11814.
- [13] Gill, Douglas M., et al. "CMOS-compatible Si-ring-assisted Mach–Zehnder interferometer with internal bandwidth equalization." Selected Topics in Quantum Electronics, IEEE Journal of 16.1 (2010): 45-52.

- [14] Watts, Michael R., et al. "Low-voltage, compact, depletion-mode, silicon Mach-Zehnder modulator." *IEEE Journal of Selected Topics in Quantum Electronics* 16.1 (2010): 159-164
- [15] Zheng, Xuezhe, et al. "A tunable 1x4 silicon CMOS photonic wavelength multiplexer/demultiplexer for dense optical interconnects." *Optics express* 18.5 (2010): 5151-5160.
- [16] Tan, Dawn Tse Hui, et al. "Wide bandwidth, low loss 1 by 4 wavelength division multiplexer on silicon for optical interconnects." *Optics express* 19.3 (2011): 2401-2409.
- [17] Dai, Daoxin, et al. "Low-loss Si₃N₄ arrayed-waveguide grating (de) multiplexer using nano-core optical waveguides." *Optics express* 19.15 (2011): 14130-14136.
- [18] Nishi, Hidetaka, et al. "Monolithic integration of a silica AWG and Ge photodiodes on Si photonic platform for one-chip WDM receiver." *Optics express* 20.8 (2012): 9312-9321.
- [19] Shoji, T., et al. "Low loss mode size converter from 0.3 μm square Si wire waveguides to singlemode fibres." *Electronics Letters* 38.25 (2002): 1669-1670.
- [20] V. R. Almeida, R. R. Panepucci, and M. Lipson, "Nanotaper for compact mode conversion," *Opt. Lett.*, vol. 28, no. 15, pp. 1302–1304, Aug. 2003.

- [21] Van Laere, Frederik, et al. "Compact focusing grating couplers for silicon-on-insulator integrated circuits." *Photonics Technology Letters, IEEE* 19.23 (2007):1919-1921.
- [22] Vermeulen, Diedrik, et al. "High-efficiency fiber-to-chip grating couplers realized using an advanced CMOS-compatible silicon-on-insulator platform." *Optics express* 18.17 (2010): 18278-18283.
- [23] Bauters, Jared F., et al. "Ultra-low-loss high-aspect-ratio Si₃N₄ waveguides." *Optics express* 19.4 (2011): 3163-3174.
- [24] Duchesne, David, et al. "Efficient self-phase modulation in low loss, high index doped silica glass integrated waveguides." *Optics express* 17.3 (2009): 1865-1870.
- [25] Xiong, Chi, Wolfram HP Pernice, and Hong X. Tang. "Low-loss, silicon integrated, aluminum nitride photonic circuits and their use for electro-optic signal processing." *Nano letters* 12.7 (2012): 3562-3568.
- [26] Jung, Hojoong, et al. "Optical frequency comb generation from aluminum nitride microring resonator." *Optics letters* 38.15 (2013): 2810-2813.
- [27] B. Rangarajan, A. Kovalgin, K. Wörhoff, and J. Schmitz, "Low-temperature deposition of high-quality silicon oxynitride films for CMOS-integrated optics," *Opt. Lett.* 38, 941-943 (2013).
- [28] G. Li, J. Yao, H. Thacker, A. Mekis, X. Zheng, I. Shubin, Y. Luo, J. Lee, K. Raj, J. Cunningham, and A. Krishnamoorthy, "Ultralow-loss, high-density SOI

optical waveguide routing for macrochip interconnects," *Opt. Express* 20, 12035-12039 (2012).

[29] K. Hammani, M. Ettabib, A. Bogris, A. Kapsalis, D. Syvridis, M. Brun, P. Labeye, S. Nicoletti, D. Richardson, and P. Petropoulos, "Optical properties of silicon germanium waveguides at telecommunication wavelengths," *Opt. Express* 21, 16690-16701 (2013)

[30] LIPKA, T. et al. Low-loss multilayer compatible a-Si:H optical thin films for photonic applications. *Journal of the European Optical Society - Rapid publications, Europe*, v. 7, aug. 2012. ISSN 1990-2573

[31] Third-order nonlinearities in silicon at telecom wavelengths
Dinu, M. and Quochi, F. and Garcia, H., *Applied Physics Letters*, 82, 2954-2956 (2003).

[32] Liang, T. K., and H. K. Tsang. "Role of free carriers from two-photon absorption in Raman amplification in silicon-on-insulator waveguides." *Applied physics letters* 84.15 (2004): 2745-2747.

[33] B. Kuyken, H. Ji, S. Clemmen, S. Selvaraja, H. Hu, M. Pu, M. Galili, P. Jeppesen, G. Morthier, S. Massar, L. Oxenløwe, G. Roelkens, and R. Baets, "Nonlinear properties of and nonlinear processing in hydrogenated amorphous silicon waveguides," *Opt. Express* 19, B146-B153 (2011)

[34] PHOTOEMISSION OF ELECTRONS AND HOLES INTO SILICON NITRIDE Goodman, Alvin M., *Applied Physics Letters*, 13, 275-277 (1968)

- [35] Del'Haye, P., et al. "Optical frequency comb generation from a monolithic microresonator." *Nature* 450.7173 (2007): 1214-1217.
- [36] Savchenkov, Anatoliy A., et al. "Tunable optical frequency comb with a crystalline whispering gallery mode resonator." *Physical review letters* 101.9 (2008): 093902.
- [37] Foster, Mark A., et al. "Silicon-based monolithic optical frequency comb source." *Optics express* 19.15 (2011): 14233-14239.
- [38] Okawachi, Yoshitomo, et al. "Octave-spanning frequency comb generation in a silicon nitride chip." *Optics letters* 36.17 (2011): 3398-3400.
- [39] Liang, W., et al. "Generation of near-infrared frequency combs from a MgF₂ whispering gallery mode resonator." *Optics letters* 36.12 (2011): 2290-2292.
- [40] Papp, Scott B., and Scott A. Diddams. "Spectral and temporal characterization of a fused-quartz-microresonator optical frequency comb." *Physical Review A* 84.5 (2011): 053833.
- [41] Ferdous, Fahmida, et al. "Spectral line-by-line pulse shaping of on-chip microresonator frequency combs." *Nature Photonics* 5.12 (2011): 770-776.
- [42] Herr, T., et al. "Universal formation dynamics and noise of Kerr-frequency combs in microresonators." *Nature Photonics* 6.7 (2012): 480-487.
- [43] Saha, Kasturi, et al. "Modelocking and femtosecond pulse generation in chip-based frequency combs." *Optics express* 21.1 (2013): 1335-1343.

- [44] Kippenberg, Tobias J., Ronald Holzwarth, and S. A. Diddams. "Microresonator-based optical frequency combs." *Science* 332.6029 (2011): 555-559.
- [45] Clemmen, Stéphane, et al. "Continuous wave photon pair generation in silicon-on-insulator waveguides and ring resonators." *Optics express* 17.19 (2009): 16558-16570.
- [46] Okawachi, Yoshitomo, et al. "Octave-spanning frequency comb generation in a silicon nitride chip." *Optics letters* 36.17 (2011): 3398-3400.
- [47] Jiang, Wei C., et al. "A silicon-chip source of bright photon-pair comb." *arXiv preprint arXiv:1210.4455* (2012).
- [48] Marcatili, Enrique AJ. "Dielectric rectangular waveguide and directional coupler for integrated optics." *Bell System Technical Journal* 48.7 (1969): 2071-2102.
- [49] Miller, Stewart E. "Integrated optics: an introduction." *Bell System Technical Journal* 48.7 (1969): 2059-2069.
- [50] P. Tien, "Light Waves in Thin Films and Integrated Optics," *Appl. Opt.* 10, 2395- 2413 (1971).
- [51] Clifford Pollock, Michal Lipson, "Integrated Photonics", Kluwer Academic Publishers 2003.
- [52] RSoft Photonics, C. A. D. "Suite, BeamPROP, FullWave."

- [53] Bååk, Tryggve. "Silicon oxynitride; a material for GRIN optics." *Applied optics* 21.6 (1982): 1069-1072.
- [54] Little, Brent E., et al. "Microring resonator channel dropping filters." *Lightwave Technology, Journal of* 15.6 (1997): 998-1005.
- [55] Klein, Edwin J., et al. "Reconfigurable optical add-drop multiplexer using microring resonators." *Photonics Technology Letters, IEEE* 17.11 (2005): 2358-2360.
- [56] Barwicz, Tymon, et al. "Microring-resonator-based add-drop filters in SiN: fabrication and analysis." *Optics express* 12.7 (2004): 1437-1442.
- [57] Popović, Miloš A., et al. "Multistage high-order microring-resonator add-drop filters." *Optics letters* 31.17 (2006): 2571-2573.
- [58] Xia, Fengnian, et al. "Ultra-compact high order ring resonator filters using submicron silicon photonic wires for on-chip optical interconnects." *Optics express* 15.19 (2007): 11934-11941.
- [59] Xia, Fengnian, Lidija Sekaric, and Yurii Vlasov. "Ultracompact optical buffers on a silicon chip." *Nature photonics* 1.1 (2007): 65-71.
- [60] Maleki, L., et al. "Tunable delay line with interacting whispering-gallery-mode resonators." *Optics letters* 29.6 (2004): 626-628.
- [61] Krioukov, E., et al. "Sensor based on an integrated optical microcavity." *Optics letters* 27.7 (2002): 512-514.

- [62] Ksendzov, A., and Y. Lin. "Integrated optics ring-resonator sensors for protein detection." *Optics letters* 30.24 (2005): 3344-3346.
- [63] Schweinsberg, Aaron, et al. "An environmental sensor based on an integrated optical whispering gallery mode disk resonator." *Sensors and Actuators B: Chemical* 123.2 (2007): 727-732.
- [64] O. Schwelb, "Generalized analysis for a class of linear interferometric networks. I. Analysis," in *IEEE Transactions on Microwave Theory and Techniques*, vol. 46, no. 10, pp. 1399-1408, Oct 1998
- [65] Xia, Fengnian, Lidija Sekaric, and Yurii A. Vlasov. "Mode conversion losses in silicon-on-insulator photonic wire based racetrack resonators." *Optics express* 14.9 (2006): 3872-3886.
- [66] Hong, S., et al. "Measuring stiffnesses and residual stresses of silicon nitride thin films." *Journal of Electronic Materials* 19.9 (1990): 903-909.
- [67] French, P. J., et al. "Optimization of a low-stress silicon nitride process for surface-micromachining applications." *Sensors and Actuators A: physical* 58.2 (1997): 149-157.
- [68] French, P. J., et al. "Optimization of a low-stress silicon nitride process for surface-micromachining applications." *Sensors and Actuators A: physical* 58.2 (1997): 149-157.

- [69] Alexander Gondarenko, Jacob S. Levy, and Michal Lipson, "High confinement micron-scale silicon nitride high Q ring resonator," *Opt. Express* 17, 11366-11370 (2009).
- [70] Schaepkens, M., et al. "Study of the SiO₂-to-Si₃N₄ etch selectivity mechanism in inductively coupled fluorocarbon plasmas and a comparison with the SiO₂-to-Si mechanism." *Journal of Vacuum Science & Technology A* 17.1 (1999): 26-37.
- [71] Mele, T. C., J. Nulman, and J. P. Krusius. "Selective and anisotropic reactive ion etch of LPCVD silicon nitride with CHF₃ based gases." *Journal of Vacuum Science & Technology B* 2.4 (1984): 684-687.
- [72] Standaert, T. E. F. M., et al. "Role of fluorocarbon film formation in the etching of silicon, silicon dioxide, silicon nitride, and amorphous hydrogenated silicon carbide." *Journal of Vacuum Science & Technology A* 22.1 (2004): 53-60.
- [73] Pan, Paihung, and Wayne Berry. "The Composition and Physical Properties of LPCVD Silicon Nitride Deposited with Different NH₃/SiH₂Cl₂ Gas Ratios." *Journal of The Electrochemical Society* 132.12 (1985): 3001-3005.
- [74] Wörhoff, K., et al. "Plasma enhanced chemical vapor deposition silicon oxynitride optimized for application in integrated optics." *Sensors and Actuators A: Physical* 74.1 (1999): 9-12.

- [75] Cotler, Tina J., and Jonathan Chapple - Sokol. "High Quality Plasma - Enhanced Chemical Vapor Deposited Silicon Nitride Films." *Journal of the Electrochemical Society* 140.7 (1993): 2071-2075.
- [76] Taft, E. A. "Characterization of silicon nitride films." *Journal of the Electrochemical Society* 118.8 (1971): 1341-1346.
- [77] Guo, Junpeng, et al. "Characterization of Si₃N₄/SiO₂ planar lightwave circuits and ring resonators." *Integrated Optoelectronic Devices 2004*. International Society for Optics and Photonics, 2004.
- [78] D. T. H. Tan, K. Ikeda, P. C. Sun, and Y. Fainman, "Group velocity dispersion and self phase modulation in silicon nitride waveguides," *Appl. Phys. Lett.* **96**, 061101 (2010).
- [79] Y. Okawachi, M. R. E. Lamont, K. Luke, D. O. Carvalho, M. Yu, M. Lipson, and A. L. Gaeta, "Bandwidth shaping of microresonator-based frequency combs via dispersion engineering," *Opt. Lett.* **39**, 3535 (2014).
- [80] C. K. Madsen, G. Lenz, A. J. Bruce, M. A. Cappuzzo, L. T. Gomez, and R. E. Scotti, *IEEE Photon. Technol. Lett.* **11**, 1623 (1999).